JOURNAL OF GEOPHYSICAL RESEARCH, VOL. ???, XXXX, DOI:10.1029/,

High-resolution Interseismic Velocity Data Along the San Andreas Fault From GPS and InSAR

X. Tong,[1] D. T. Sandwell,[1] B. Smith-Konter,[2]

X. Tong, Institution of Geophysics and Planetary Physics, Scripps Institution of Oceanography, University of California, San Diego, 8800 Biological Grade, San Diego, CA 92037-0225, USA. (xitong@ucsd.edu)

D. T. Sandwell, Institution of Geophysics and Planetary Physics, Scripps Institution of Oceanography, University of California, San Diego, 8800 Biological Grade, San Diego, CA 92037-0225, USA. (dsandwell@ucsd.edu)

B. Smith-Konter, Department of Geological Sciences, University of Texas at El Paso, El Paso, Texas, 79968-0555 USA. (brkonter@utep.edu)

[1]Institution of Geophysics and Planetary Physics, Scripps Institution of Oceanography, University of California, San Diego, USA

[2]Department of Geological Sciences, University of Texas at El Paso, El Paso, Texas, USA.

Abstract. We compared 4 interseismic velocity models of the San Andreas Fault (SAF) based on GPS observations [*Mccaffrey*, 2005; *Meade and Hager*, 2005a; *Smith-Konter and Sandwell*, 2009; *Zeng and Shen*, 2010]. The standard deviations of the 4 models are larger north of the Bay Area, near the Creeping segment in Central California, and along the San Jacinto fault and the East California Shear Zone in Southern California. A coherence spectrum analysis indicates relatively high correlation among the 4 models at longer wavelengths (>15-40 km), with lower correlation at shorter wavelengths. To improve the short-wavelength accuracy of the interseismic velocity model, we integrated InSAR observations, initially from ALOS ascending data (spanning from the middle of 2006 to the end of 2010, totaling more than 1100 interferograms), using a Sum/Remove/Filter/Restore (SURF) approach. The final InSAR line-of-site (LOS) data match the point GPS observations with a mean absolute deviation of 1.3 mm/yr. We systematically evaluated the fault creep rates along major faults of the SAF and compared them with creepmeters and alignment array data compiled in UCERF2. Moreover, this InSAR LOS dataset can constrain rapid velocity gradients near the faults, which are critical for understanding the along-strike variations in stress accumulation rate and associated earthquake hazard.

1. Introduction

The San Andreas Fault (SAF) System is northwest trending transform plate boundary between the North America and Pacific plates. Major geological fault traces along the SAF are shown in Figure 1 in an oblique Mercator projection. The plate velocity between the North America and Pacific plates is about 45 mm/yr, determined from global plate motion models [*Demets et al.*, 1994, 1990]. In Central California, the geological and geodetic slip rates of the SAF consistently suggest that 70-80% of the plate motion is accommodated by the SAF [*Noriega et al.*, 2006; *Rolandone et al.*, 2008]. In Southern California, the SAF splays into three main branches, the Elsinore fault, the San Jacinto fault, and the San Andreas Fault, which distribute about 45 mm/yr of strike-slip motion over a 200 km region. To the north of the Creeping section, the SAF diverges offshore slipping at 25 mm/yr, while the paralleling Hayward and Calaveras faults absorb about 8 mm/yr of the dextral wrenching motion [*Lienkaemper and Borchardt*, 1996; *Segall*, 2002]. A recent summary of the geological and geodetic slip rates of the SAF can be found in *Molnar and Dayem* [2010].

GPS measurements across the North American - Pacific Plate boundary are providing decade and longer time-series at 2 to 3 millimeter-level precision from which surface velocity estimates are derived. One of the goals of these models is to provide strain rate estimation and to forecast seismicity rate. Several geodetic research groups have used these point velocity measurements to construct large-scale maps of crustal velocity. Since the typical spacing of GPS stations is about 5-10 km, an interpolation method or physical model must be used to compute a continuous vector velocity model that can be differentiated to construct a strain-rate map. Four approaches are typically used to develop strain maps: isotropic interpolation, interpolation guided by known faults, interpolation of a rheologically-layered lithosphere, and analytically determined strain rates derived from a geodetically constrained block model in an elastic half space.

The earliest interpolation studies used discrete GPS observations directly to obtain a spatially continuous horizontal velocity field and strain rate [*Frank*, 1966; *Shen et al.*, 1996]. This method makes no assumptions on the location of a fault and does not need to solve for fault slip rates and locking depths when characterizing the strain field. Unknown faults (e.g. blind thrust faults), if accommodating enough strain, might be manifested through this method. *Freed et al.* [2007] explored the relationship between occurrence of the $M>6$ earthquakes and the stress changes induced by coseismic, postseismic, and interseismic deformation. Their interseismic stress accumulation rates were calculated directly from SCEC Crustal Motion Map (CMM3). *Kreemer et al.* [2003] constructed a global model for horizontal velocity and horizontal strain rate over major plate boundaries. They derived the velocity field from a least-squares interpolation method using bi-cubic Bessel splines. *Hackl et al.* [2009] developed a new interpolation procedure to compute strain directly from dense GPS networks and applied it to the interseismic deformation in Southern California and coseismic deformation of earthquakes. While these approaches have produced "nice" maps of the 1st order strain rate field, the main issue is that in places where fault location information is not used, the spacing of GPS data is insufficient to accurately map the high strain concentrations along major faults.

The second main strain rate modeling approach uses GPS observations to constrain fault slip rate and locking depths through model parameterization assuming a known set of fault locations. In these studies, model parameters are usually derived from minimization of the residual between the GPS observations and model prediction. An incomplete list of these models follows: *Mccaffrey* [2005] represented the active deformation of southwestern United States with rotating, elastic-plastic spherical caps. *Meade and Hager* [2005b, a] estimated the moment accumulation rate from an elastic block model of interseismic deformation on the SAF constrained by GPS measurements. *Smith-Konter and Sandwell* [2009] used a semi-analytic viscoelastic earthquake cycle model to simulate the moment accumulation rate and stress evolution of the SAF over a thousand years[*Smith and Sandwell*, 2003, 2004, 2006]. *Shen and Jackson* [2005] modeled the surface deformation of Southern California using an elastic block model, which did not strictly enforce the continuity of fault slip rate on adjacent fault segments. *Parsons* [2006] constructed a finite element model of California by considering surface GPS velocity, crustal thickness, geothermal gradient, topography, and creeping faults. *Bird* [2009] incorporated community geologic, geodetic, and stress direction data to constrain the long-term fault slip rates and distributed deformation rates with a finite element model. It is worth noting that a deep dislocation underneath active faults is not a unique representation of the strain accumulation pattern everywhere in California. It has been proposed that the geodetic data may be explained to first order by simple shear across an 135-km-wide shear zone [*Savage et al.*, 1998; *Pollitz and Nyst*, 2005] in the San Francisco Bay region.

A recent analysis of 17 strain-rate models for the SAF has shown that GPS data alone cannot uniquely resolve the rapid velocity gradients near faults [*Hearn et al.*, 2010]. The standard deviation of the strain models reveals a large discrepancy close to the fault, which can be caused by the different interpolation schemes used in constructing the strain models from discrete GPS measurements. *Baxter et al.* [2011] investigated the techniques to derive strain from discrete GPS velocity vectors and its inherent limitations. Incorporating Interferometric Synthetic Aperture Radar (InSAR) data along with GPS data has proven to be important to constrain high resolution kinematics over the tectonically active region [*Fialko*, 2006; *Wei et al.*, 2009].

In this paper we first evaluate the mean and standard deviation of 4 independent models to show that the GPS-derived interseismic velocity models are coherent at wavelengths greater than 15-40 km. Second, we develop a method to integrate InSAR data with GPS observations to recover the high-resolution interseismic velocity of the SAF. Third, we evaluate errors in the InSAR Line-Of-Sight (LOS) data by comparing it to GPS measurements. (The InSAR LOS data and their uncertainties are available at `ftp://topex.ucsd.edu/pub/SAF_model/insar`). Finally, we use this dataset to estimate the fault creep rates along the SAF and other major faults systematically and compare these estimation with 115 ground-truth observations such as creepmeters and alignment arrays.

2. Evalution of interseismic velocity models based on GPS measurements

To establish the accuracy and resolution of available interseismic velocity models, we compared 4 independent models based primarily on GPS observations. The models are:

H-model: *Meade and Hager* [2005a] developed a block model of Southern California constrained by the SCEC CMM3 GPS velocity. This was refined by *Loveless and Meade* [2011]. Their block models considered the block rotation and both the fault-parallel and fault-normal steady-state slip on block-bounding faults. They estimated the effective locking depths on some of the fault segments, and used results from previous studies on other fault segments.

M-model: *Mccaffrey* [2005] represented active deformation of the southwestern United States with rotating, elastic-plastic spherical caps. The GPS velocity field was modeled as a result of rigid block rotations, elastic strain on block-bounding faults, and slip on faults within blocks (i.e. permanent strain).

Z-model: *Zeng and Shen* [2010] inverted regional GPS observations to constrain slip rates on major faults in California based on Okada solutions. Their model simulates both block-like deformation and elastic strain accumulation.

S-model: *Smith-Konter and Sandwell* [2009] developed a 3-D semi-analytic viscoelastic model to simulate the full earthquake cycle including interseismic deformation, coseismic displacement from past earthquakes, and postseismic relaxation following earthquakes. The slip rate was adopted from geologic studies and the apparent locking depth was estimated from the regional GPS velocity field. The model is fully 3-D and the vertical component of the GPS vectors is also used in the adjustment. In this study we improve the original model by adding a grid of residual velocity using a spline fitting method [*Hackl et al.*, 2009].

We use two approaches to establish the similarities and differences among these 4 models. First we compute the mean and standard deviations of the horizontal components of the models and then we evaluate the spectral coherence among the models.

2.1. Standard deviations

Figure 2 shows the mean velocity and standard deviations of the 4 different GPS models. All the models are gridded at 0.01-degree pixel spacing with the *GMT surface* command.

We adjusted each velocity model by subtracting its mean so that they reflect the same reference. The mean value of these models (2.5 mm/yr contour interval) shows a right lateral shear along the SAF and the East California shear zone and transpression motion over the Mojave segment of SAF. At the Creeping section, the velocity changes sharply, indicating a low degree of coupling of the fault, while in Southern and Northern California, the right lateral shear motion is taken up by multiple parallel faults. The standard deviation (0.5 mm/yr contour interval) ranges from 0 to 2 mm/yr for both the east and north velocity, except for at the Creeping section where it exceeds 3 mm/yr. The smaller standard deviation (<1.0 mm/yr) indicates good agreement among models and larger standard deviation (>1.0 mm/yr) emphasizes the areas of largest discrepancy, such as the Creeping section, north of the Bay Area, the San Jacinto fault and the East California Shear Zone in Southern California. A similar kind of effort to compare independent model results has been carried out in a previous California strain rate comparison [*Hearn et al.*, 2010].

There are several factors that could explain the discrepancy among the GPS models. First, the discrepancy could be caused by the imprecise location of a fault or inaccurate fault dip, which could be resolved by using a more precise fault model. On the Creeping part of the SAF (e.g. Hayward fault, Calaveras fault, Creeping sections over Central California), the fault trace could be more accurately constrained by velocity steps revealed by InSAR observations. Second, the discrepancy could be caused by different locking depth and slip rate used in different models. As shown in Figure 2, there is a larger uncertainty among the models north of the Bay area. For example, *Mccaffrey* [2005] used a 7.4 mm/yr slip rate with 1-2 km locking depth on the Maacama fault while *Smith-Konter* *and Sandwell* [2009] used a 10 mm/yr slip rate and 8.6 km locking depth. Likewise, 30 km east of the Maacama fault resides the Green Valley fault. *Mccaffrey* [2005] used a 7.3 mm/yr slip rate with very shallow locking (1-2 km) [*Mccaffrey*, 2005, Figure 3a]. *Smith-Konter and Sandwell* [2009] used a slip rate of 6.4 mm/yr with a locking depth 5 km. This analysis illustrates that the current GPS velocity field is not able to distinguish a shallow locked fault from a creeping fault. For instance, we calculated two fault-parallel velocity profiles by changing the locking depth from 1 km to 5 km, for a constant slip rate of 7 mm/yr. The difference of the velocity profiles reaches a maximum of 1.6 mm/yr at 2 km from the fault trace and decreases to 0.2 mm/yr at 40 km from the fault. Thus high resolution and high precision observations close to the fault are needed to constrain the slip rates and locking depths of paralleling faults. Third, in the area where significant surface creep occurs, like the Creeping section in Central California, the locking depth is difficult to constrain from GPS alone.

2.2. Cross-spectrum analysis

The second method used to establish the similarities and differences among these 4 models was to perform a cross-spectral analysis among pairs of models (Figure 3). Based on the above analysis, we expect the model pairs to show good agreement at longer wavelengths and poor agreement at shorter wavelengths. In particular, we want to establish the shortest wavelength where the models are in agreement at 0.5 coherence. This crossover wavelength is needed to determine the filter wavelength in the GPS/InSAR integration step. We used the Welchs modified periodogram approach [*Welch*, 1967] as implemented in MATLAB to estimate coherence for 37 LOS profiles crossing the plate boundary. There are three steps in this approach:

1. Project horizontal velocity components into the LOS velocity for each of the 4 GPS models.

2. Extract across-fault profiles spaced at 10-20 km intervals in the north-south direction. Each profile starts at the coastline and extends 300 km inland. The profiles that have gaps (no data) are discarded. We extract 37 profiles from each model (transect lines in Figure 3a) with a sampling spacing for each profile of 0.2 km.

3. Concatenate the 37 profiles end-to-end to form one vector for each model. Compute the magnitude-squared coherence using Welch's averaged periodogram method. In order to avoid artifacts associated with jumps where the 37 profiles abut each other, we first applied a 300 km long hanning-tapered window to each profile. Then the periodogram for the 37 profiles were computed and averaged to get the final estimate of the coherence spectrum.

Figure 3b shows the coherence as a function of wavenumber for all the possible combinations within the 4 GPS models. Because the profiles only sample 300 km in across-fault distance, the coherence estimated over wavelengths greater than 150 km is not reliable. Below 150 km wavelengths however, the coherence estimates show several interesting features: To first order, the coherence among GPS models is high (>0.8) between wavelengths of 150 and 66 km and then drops to 0.5 at about 20 km wavelengths. This wavelength is expected because it corresponds to the characteristic spacing of the GPS receivers. There is a high coherence of 0.8 at the 33-50 km wavelength among Z, H and S models. In contrast, the coherence between M-model and other models has a relatively low value of 0.55 at the same scale. While all the other models show lower correlation at smaller length scales, the correlation between Z-model and H-model reaches 0.9 between wavelengths of

1 and 10 km. We suspect that this high coherence reflects the fact that these two models use nearly identical fault geometry and have short wavelength signal that is common at creeping faults. We found that the averaged coherence spectrum falls off to 0.5 at approximately 17 km (Figure 3c). This crossover wavelength will be used in the GPS/InSAR integration as discussed in next section.

3. Integration of InSAR and GPS

The approach for combining multiple interferograms of a region with GPS observations has 4 primary steps and is based on a study by *Wei et al.* [2010]. The first step is to sum up the available interferograms, keeping track of the total time span of the sum to compute a line-of-sight (LOS) velocity. This stacking will enhance the signal-to-noise ratio because, for example, the residual tropospheric noise is uncorrelated for a time span longer than 1 day [*Williams et al.*, 1998; *Emardson et al.*, 2003]. The second step is to project an interseismic velocity model based on the GPS measurements into the line-of-sight (LOS) velocity of the interferogram (Figure 4) and to remove this model from the stack. For this study we use a modified version of the S-model to provide a long-wavelength basis for integration of GPS and InSAR. The horizontal components of this velocity model are used in the projection. The third step is to high-pass filter the residual stack to further suppress errors with lengths scales much greater than the crossover wavelength. This crossover wavelength was selected based on the coherence analysis above. The final step is to add the GPS-based model back to the filtered stack to recover the full LOS velocity. The acronym for this integration approach is called "SURF" (Sum/Remove/Filter/Restore). As shown in Figure 5, it is clear that the recovered InSAR LOS velocity map provides shorter wavelength information not captured by the GPS-based model (compare to Figure 4). The details of the result shown in Figure 5 are discussed in Section 4.

3.1. InSAR data processing

We processed 13 ascending tracks of ALOS PALSAR interferograms spanning from the middle of 2006 to the end of 2010 in preparation for stacking. More than 1100 interferograms were processed to cover the entire SAF. We performed the InSAR data processing and the GPS/InSAR integration using GMTSAR software, which is publicly available from `http://topex.ucsd.edu/gmtsar` [*Sandwell et al.*, 2011]. We processed the SAR data on a frame-by-frame basis so that the frame boundaries of the interferograms match seamlessly along track (Figure 5). By doing so, we avoided discarding entire tracks of data and still processed other frames along the same track if the pulse repetition frequency (PRF) changes along track or the SAR data in one of the frames were missing or problematic. A summary of the SAR dataset used in the analysis is in Table 1.

The main processing steps are (1) pre-processing, (2) SAR image formation and alignment, (3) interferograms formation and topographic phase correction, (4) phase unwrapping, (5) GPS/InSAR integration. We discuss details of steps 2) to 5) in the following paragraphs. All of these steps are done in the radar coordinates for consistency. After GPS/InSAR integration, we projected the products into geographic coordinates with pixel spacing of 3 arc seconds ($\sim$90 meters) for further analysis.

As shown in an example baseline-time plot (Figure 6), the perpendicular baseline of the ALOS satellite drifted from -1000 m to 1000 m (2007 June -2008 April) and then was reset to -7000 m in the middle of 2008, when it then started to drift again. Subsequently, short baseline and long time-span interferograms were not available until the middle of

2010. Unfortunately the satellite stopped working due to power issue in April 2011, so for most frames, fewer than 20 interferograms are available for stacking. The drifting orbit also makes it difficult to align all the images using conventional methods.

As shown in Figure 6, the baseline between the two SAR images can reach several thousand meters, thus a direct alignment of the images relying on the satellite trajectory is difficult. We adopted a "leap frog" approach [*Sandwell and Sichoix*, 2000; *Sandwell et al.*, 2011] to align every image in this baseline-time plot to one image (called "super master"). Taking Figure 6 as an example, we first chose an image as "super master" (10024 in this case). We then aligned the images that were close to (i.e. perpendicular baseline <1000 m) the"super master" in the baseline-time domain to the"super master" (marked as Primary match in Figure 6). After alignments, the images were registered in the same coordinates as the"super master" within one pixel accuracy, thus they can be treated as new master images (called "surrogate master"). Then we aligned other images (marked as Secondary match in Figure 6) that are far from the "super master" in the baseline-time domain to the"surrogate master".

Because the interseismic motion is subtle compared to the atmospheric noise, we chose interferometry pairs with long time intervals (>1 yr) and with small perpendicular baselines (<600 m) to enhance the signal to noise ratio (Figure 7). The summations of the perpendicular baselines are minimized to reduce the topographic error (Table 1). Topographic phase is removed using digital elevation model (DEM) SRTM1 [*Farr et al.*, 2007]. The relative height error of SRTM over North America is estimated to be 7 meters. In addition, the height measured by SRTM is an effective height. In the presence of vegetation or snow or very dry soil, C-band radar waves on board SRTM reflected at a different effective height than the L-band radar on board ALOS, which can cause an error in DEM on the order of 5-10 meters. The relationship between LOS velocity error dv and the DEM error dh after stacking is: $dv = \frac{4\pi}{\lambda} \frac{\sum B^i_{perp}}{\sum_{i=1}^{N} \Delta t^i} \times \frac{r_e+h}{\rho b \sin\theta} dh$ [*Sandwell et al.*, 2011, Appendix C] , where r_e is radius of the Earth (6371 km), ρ is the distance from the radar satellite to the ground (800 km), b is the distance from the radar satellite to the center of the Earth (7171 km), λ is the radar wavelength (0.236 m), h is the elevation of the ground (1 km), θ is the radar look angle (34°), i denotes the ith interferogram, N is the total number of interferograms, $\frac{\sum B^i_{perp}}{\sum_{i=1}^{N} \Delta t^i}$ is the summation of perpendicular baseline over the summation of the time span for all the interferograms (10m/10,000 days). See Table 1 for exact values used in the data processing. Using the above representative values denoted in the parenthesis and taking DEM error dh to be 10 meters, we calculated a bias in LOS velocity dv of 0.4 mm/yr. The interferograms were filtered with a Gaussian low-pass filter at 200 meters full wavelength and subsequently subsampled at 2 pixels in range (15.6 meters projected on the ground) by 4 pixels in azimuth (13.2 meters). We then applied a Goldstein filter [*Goldstein and Werner*, 1998] to the interferograms to obtain the final interferogram in wrapped phase.

In order to identify the small-scale deformation signal, one wants to eliminate the errors associated with the automatic unwrapping. Sometimes automatic unwrapping provide inaccurate results (known as“phase jumps”), especially where there are cultivated fields, sand dunes, or water. We devised an iterative approach to overcome difficulties that occasionally occur in automatic phase unwrapping of InSAR phase data (Figure 8). Initially, we unwrapped the phase of each interferogram using SNAPHU software [*Chen and Zebker*, 2000]. Next, we constructed a trend from the unwrapped phase using *GMT* *functions grdtrend, grdfilter, surface.* Then we removed it from the original wrapped phase to derive the fluctuation phase. If the fluctuation phase is within $\pm\pi$, we add fluctuation to the trend to get a complete unwrapped phase and the unwrapping is done; If not, we re-estimate the trend and iterate. We unwrapped the phase by hand for some extremely difficult cases, like the interferograms over the Imperial Valley.

3.2. The SURF approach

After unwrapping the phase of each interferogram, we carried out the GPS/InSAR integration step using the SURF approach [*Wei et al.*, 2010] shown as Figure 9. We discuss the advantages of this integration approach in section 3.3. Here we describe each step in detail:

1. **Sum** the unwrapped phase of each interferogram $\phi^i(x, \Delta t^i)$, i denotes the ith interferogram, x is a 2 dimensional spatial variable in radar coordinates. Scale the summation with respect to their corresponding time interval Δt^i using formula $\overline{\phi}(x) = \frac{\sum_{i=1}^{N} \phi^i(x, \Delta t^i)}{\sum_{i=1}^{N} \Delta t^i}$, and convert it into LOS velocity. N is the total number of interferograms. Make a coherence mask (>0.06) from a stack of coherence maps using formula $\overline{\gamma} = \frac{1}{\sqrt{\frac{1}{N}\sum_{i=1}^{N}\frac{1}{\gamma_i^2(x)}}}$, where $\gamma_i(x)$ is the coherence map for the ith interferogram. Make a land mask if applicable. Make a mask to isolate the anomalous deformation signals when necessary.

2. **Remove** the GPS model $M(x)$ from the stacked phase to obtain the residual phase by $\overline{\phi}(x) - M(x)$, where $M(x)$ is the interseismic velocity model from GPS. The interseismic velocity model *Smith-Konter and Sandwell* [2009] is projected from geographic coordinates (longitude-latitude) into radar coordinates (range-azimuth). The 2-components (local East-North) velocity of each pixel is converted into Line-Of-Sight (LOS) velocity considering variable radar looking directions across track (Figure 4).

3. **Filter** the residual phase with a Gaussian high-pass filter $F_{high}(x)$ at the crossover wavelength by $[\overline{\phi}(x) - M(x)] * F_{high}(x)$. *Wei et al.* [2010] used a crossover wavelength of 40 km uniformly inferred from typical spacing of GPS sites. We determined the filter wavelength based on a coherence spectrum analysis and found that 17 km was an optimal crossover wavelength of the GPS models. The optimal crossover wavelength may vary from location to location and warrants further investigation. The high-pass filtered residual $[\overline{\phi}(x) - M(x)] * F_{high}(x)$ shows the small-scale difference between the InSAR LOS velocity and the GPS model prediction (Figure 10).

4. **Restore** the original interseismic velocity model $M(x)$ by adding it back to the filtered residual phase. Thus $V_{InSAR}(x)$ combines the short wavelength signal from InSAR stacking and the long wavelength signal from GPS. Convolution is a linear operator, thus we have: $V_{InSAR}(x) = [\overline{\phi}(x) - M(x)] * F_{high}(x) + M(x) = \overline{\phi}(x) * F_{high}(x) + M(x) * F_{low}(x)$. $F_{low}(x)$ is the corresponding low-pass filter. The error from the GPS-based model after low-pass filtering is reduced to a level of 1 mm/yr as discussed in Section 2, and the error from InSAR after high-pass filtering is evaluated in step 5.

5. We evaluated the errors in the InSAR data after high-pass filtering by calculating its standard deviations with formula $\sigma_{InSAR}(x) = \frac{\sum_{i=1}^{N}\{[\frac{\phi^i(x,\Delta t^i)}{\Delta t^i} - V_{InSAR}(x)] * F_{high}(x)\}^2}{N}$ (Figure 11). Larger uncertainties could be due to unwrapping errors, atmospheric noise or non-steady-state ground motion. The standard deviation varies spatially ranging from 1 mm/yr to > 10 mm/yr for some regions with average value of $\sim$3 mm/yr.

3.3. Advantage of this GPS/InSAR integration approach

Although there are not many explicit studies on GPS/InSAR integration methods, almost every study using InSAR phase data to retrieve coseismic, postseismic, interseismic and volcanic deformations relies on GPS to correct the long wavelength errors of InSAR phase data. We found that this integration method usually involves interpolation between GPS stations [*Gourmelen et al.*, 2010; *Johanson and Burgmann*, 2005; *Lyons and Sandwell*, 2003; *Peltzer et al.*, 2001; *Ryder and Burgmann*, 2008; *Wei et al.*, 2009]. For instance *Johanson and Burgmann* [2005] studied the interseismic slip rate on the San Juan Bautista segments of the SAF. For each interferogram, they removed a GPS-derived interseismic velocity model from interferogram phase data to obtain the so-called residual phase, then they fitted and removed a lower-order polynomial from the residual phase, then they replaced the interseismic model back. The removal of an interseismic velocity model may facilitate phase unwrapping. We call this kind of integration approach remove/correct/restore/stack method. *Wei et al.* [2009] used a very similar method but their procedure is remove/stack/correct/restore. The exact order of the processing steps does not matter much because of the linearity of these operations. In other studies the difference between the interferogram phase data and the co-located GPS measurements are used to construct a linear trend, which is subsequently removed from the InSAR phase data [*Fialko*, 2006; *Lundgren et al.*, 2009].

In this study we used the SURF approach to integrate GPS and InSAR observations. This simple approach is an improvement based on the aforementioned method: the remove/correct/restore/stack method that has been used extensively. Our approach has the following characteristics: 1) this method does not assume a particular form of the orbital error because the exact form of the first- or second-order polynomial is uncertain [*Gourmelen et al.*, 2010]. 2) The interpolation between GPS stations is realized by a physical model constrained by GPS velocity [*Smith-Konter and Sandwell*, 2009]. 3) The high-pass filter further improves the signal to noise ratio of the stacking by filtering out tropospheric and ionospheric noise. 4) The wavelength of the high-pass filter used in this study is determined by a cross-comparison of 4 independent interseismic velocity models (Figure 3). 5) The high-pass filtered residual data provide information on the inaccuracy of the current interseismic models. This method has the potential to be applied and developed in other InSAR studies.

4. Evaluation and distribution of LOS results

4.1. InSAR LOS velocity map

Figure 5a shows the high-resolution interseismic velocity data ($V_{InSAR}(x)$) along the SAF derived from integrating the GPS observations with ALOS radar interferograms (2006.5-2010). The areas with low coherence and large standard deviation (> 6 mm/yr) are masked. Comparing this to GPS model (Figure 4), the recovered interseismic velocity data has greater variations including: surface expression of the fault creep, localized deformation pattern related to non-tectonic effect and anomalous velocity gradient near active faults. These details of the velocity field are highlighted by shading the final grid weighted by its gradient. A full resolution version of this LOS velocity map and its relationship to faults and cultural features can be downloaded as a KML-file for Google Earth from the following site: `ftp://topex.ucsd.edu/pub/SAF_models/insar/ALOS_ASC_masked.kmz`. A data file of longitude, latitude, LOS velocity, standard deviations of the LOS velocity, unit vector for LOS can be obtained through `ftp://topex.ucsd.edu/pub/SAF_model/insar`. Next we discuss two sub-regions.

Figure 5b shows the broad transition in velocity across the San Andreas and San Jacinto faults that is well studied [*Fialko*, 2006; *Lundgren et al.*, 2009]. Besides this large-scale feature, we note several interesting small-scale features. Shallow fault creep is apparent across the San Andreas (∼4 mm/yr) near the Salton Sea [*Lyons and Sandwell*, 2003], as well as across the Superstition fault (∼3 mm/yr) [*Wei et al.*, 2009]. There are several areas of rapid localized subsidence possibly due to groundwater extraction. For example, there is a large subsidence region around Indio, CA where subsidence has been documented by [*Sneed and Brandt*, 2007]. Other prominent examples of anomalous velocity occur along the Coachella valley west of the SAF where prominent subsidence at >30 mm/yr, and uplift of ∼10 mm/yr just north of the Salton Sea, is observed (see Figure 5b). There is an interesting subsidence confined by a "step-over" structure along the San Jacinto fault [*Wisely and Schmidt*, 2010]. The subsidence rate in this "step-over" reaches as high as ∼18 mm/yr, which is too large compared to the expected signal from tectonic extension. Localized subsidence is also apparent at Obsidian Butte (∼14 mm/yr) to the south of the Salton Sea [*Eneva and Adams*, 2010].

Figure 5c shows the sharp velocity gradient across the Creeping Section, as well as the Calaveras fault in central part of the SAF [*Johanson and Burgmann*, 2005]. From this map we identify the southern end of the Creeping section is at a "step-over" south to the Parkfield region (Figure 5c). We divided the Creeping section into 3 segments: northern, central, and southern segments and took profiles across the fault. Three profiles are shown in Figure 12. InSAR observations resolved the creeping signal within 10 km from the fault trace. On the northern segment, the Creeping section is creeping at ∼4 mm/yr in LOS (∼14 mm/yr in horizontal). The Paicines segment of the Calaveras fault (5 km to the east of the SAF) is also creeping at 3-4 mm/yr in LOS. On the central segment of the Creeping section, the ∼7 mm/yr creep rate in LOS (∼23 mm/yr in horizontal) is well recovered.

On the southern segment of the Creeping section, InSAR detects anomalous asymmetric ground motion within 3 km west of the fault zone. From Figure 5c, the rate of the motion is about -12 mm/yr near the fault trace and decrease to -6 mm/yr just 3 km west of the fault. The gradient associated with this LOS velocity change is 2mm/yr/km, thus if we attribute this anomaly to horizontal simple shear in the vicinity of the fault zone, the shear strain rate is 6 microstrain/yr, which is unrealistic large. Due to the ambiguity of the InSAR LOS direction, we could not detect if the ground is moving horizontally or vertically. As far as we know, this peculiar deformation signal on the Creeping section and its cause have not been understood by previous workers. Since the horizontal movement would imply unrealistically large shear strain, the vertical uplift seems a more plausible explanation. Vertical motion could be caused by fluid flow trapped within the porous brittle fault zone [*Byerlee*, 1993; *Wisely and Schmidt*, 2010]. This apparent anomaly could also be caused by the artifacts in the radar interferograms, such as a change in the surface reflective property. With additional ERS or Envisat satellite data or GPS data, it might be possible to resolve this issue.

4.2. Comparison with GPS LOS data

We compared the recovered LOS velocity $V_{InSAR}(x)$ with 1068 co-located GPS measurements to investigate the accuracy of $V_{InSAR}(x)$. We denote the projected GPS velocity vectors and their standard deviations as $V_{GPS}(x)$ and $\sigma_{GPS}(x)$. These are projected into the LOS direction using the precise orbital information from each satellite track. We divide our comparison results into two groups depending on whether the vertical velocity of the GPS vectors are included in the projection. The results are summarized in Figure 13. Figure 13a shows the histogram of the differences between the recovered LOS velocity and GPS measurements $V_{diff}(x) = V_{GPS}(x) - V_{InSAR}(x)$. The standard deviation and the mean absolute deviation of $V_{diff}(x)$ are 4.0 mm/yr and 2.3 mm/yr respectively. Figure 13c shows the scatter plot between $V_{InSAR}(x)$ and $V_{GPS}(x)$. As expected, these two measurements are linearly correlated and the normalized correlation coefficient is 0.66 (1 means perfect correlation). Figure 13e shows that the uncertainties of the two measurements $\sigma_{GPS}(x)$ and $\sigma_{InSAR}(x)$ are not correlated as their correlation coefficient is only -0.05. The estimate of $\sigma_{InSAR}(x)$ includes seasonal effects that vary annually or semi-annually but the estimate of $\sigma_{GPS}(x)$ has these effects removed. When only the horizontal components of the GPS velocity are used in the projection (Figure 13b, 13d, 13f), the standard deviation of $V_{diff}(x)$ reduces to 1.9 mm/yr, its mean absolute deviations is reduced to 1.3 mm/yr, and the correlation coefficient between GPS and InSAR measurements increases to 0.90.

Since the InSAR data contains both signal and noise, we investigated how spatial averaging can improve the signal-to-noise ratio of the LOS velocity. A common way to improve the signal-to-noise ratio is to apply a moving-average window with a designated window size. We used the *GMT blockmedian* command to average LOS velocity $V_{InSAR}(x)$ at different spatial scales then computed the standard deviations of $V_{diff}(x)$. Figure 14 shows how the standard devations of $V_{diff}(x)$ vary as a function of spatial averaging. We present both the standard deviation and the mean absolute deviation of $V_{diff}(x)$. We consider the projected LOS velocity from GPS vectors both with and without vertical component. For the comparison using horizontal components of the GPS data, the mean absolute deviation of $V_{diff}(x)$ reduces from 1.3 mm/yr to 0.9 mm/yr after spatial averaging the InSAR data at 3 arcminutes (∼6 km in distance) and remains constant for bigger average windows. For the comparison including vertical GPS velocity the spatial averaging hardly change the fit to the GPS data. As shown in Figure 14, including the vertical component of GPS velocity degraded the fit by ∼25-50% compared to the case with only horizontal components, which could be caused by larger uncertainties in the vertical component of GPS data.

4.3. Power spectrum

The InSAR data adds significant short wavelength noise and signal to the GPS-only model. We calculated the power spectrum (Figure 15a) of the GPS model and the LOS data, as well as their coherence spectrum (Figure 15b). Because estimating power spectrum requires long swaths (>250 km), 12 profiles, instead of 37 profiles, in Southern California were averaged to obtain a reasonable spectrum (marked in Figure 3a). At long wavelengths, the two spectrums are at similar magnitude but their fall-off rates differ (Figure 15a). A power-law fitting to the power spectrum suggests that the spectrum of the GPS model falls off as $f^{-5.5}$, while the spectrum of the InSAR data falls off as $f^{-1.8}$ where f is the wavenumber. Although the power in the InSAR data could also be due to noise (i.e. atmosphere and ionosphere noise), many small-scale features, such as localized subsidence and fault creep significantly contribute to the power over the short wavelengths, which could explain the difference in the fall-off rate. Figure 15b shows the coherence spectrum of the GPS model and the InSAR LOS velocity. The coherence reaches 0.95 at 100 km wavelengths, then decreases to below 0.2 at 15-40 km wavelength. This characteristic of the coherence spectrum is expected because the recovered lnSAR LOS data contains the short wavelength signal not captured by the GPS.

5. Fault creep

We used the InSAR LOS data to estimate surface fault creep rate along the SAF system. Although many previous InSAR studies have measured fault creep rate over limited areas, this analysis is the first to provide comprehensive creep rate estimates for all the major faults of the SAF system over the time interval of the ALOS data acquisition 2006.5 to 2010. In addition to estimating creep rate, we also provide uncertainties and show comparisons with ground-truth measurements (Figure 16) such as GPS, alignment arrays (AA), creepmeters (CM) and cultural offsets (Cult) *Wisely et al.* [2008]. We performed the above analysis for the SAF, Maacama fault, Bartlett Springs fault, Concord fault, Rogers Creek fault, Calaveras fault, Hayward fault, Garlock fault, San Jacinto fault, and Superstition fault. The creep rate estimates, their geographic coordinates, and their uncertainties are summarized in Table 2.

5.1. Estimating fault creep rate

Here we record the best-fit creep rate across the fault trace from InSAR LOS velocity profiles. We used the method described by *Burford and Harsh* [1980] to determine the best-fit rates. The creep rate is quantified as an offset of the intercepts of the two best-fit linear functions (Figure 16 inset) at the fault trace (0 km distance). We took profiles of the high-resolution velocity grid perpendicular to fault strike. The profiles were at 0.002 degrees intervals in longitude along fault strike. The sampling interval across the fault was 0.2 km for 1 km on either side of the fault. The centers of the profiles were carefully chosen to reflect small bending sections of the fault traces. Then we averaged the profiles every 10 km along the fault strike. For each averaged profile, there were 5 LOS velocity data points on either side of the fault. In this analysis, we assumed no vertical motion across fault. We scaled the LOS velocity into horizontal direction considering variation of the fault strike. The RMS of the residuals after linear regression was taken to be the error in the creep rate. We avoided making estimation if there were more than 2 data points missing in the averaged profiles on either side of the fault.

We then compared our estimates with the compilation of creep measurements from *Wisely et al.* [2008] from various instruments (GPS, AA, CM, Cult) along the SAF (Figure 16). It should be noted that the InSAR measurement of fault creep represents the velocity difference on a scale of 200-300 m across the fault. In contrast, creepmeters and alignment arrays measure the velocity difference over a shorter distance of typically tens of meters to ∼100 meters. Therefore, one would expect differences with the InSAR estimates bigger unless the creep is really confined to a very small distance from the fault. Also note that the time period of these measurements is usually different. The alignment array surveys are usually carried out in 1970s to 1980s and while the GPS surveys and the InSAR observations are more recent and span shorter time period. Despite these limitations, we found that the match between these independent measurements is satisfactory.

5.2. Creep rate results

The InSAR-detected surface creep rates on the SAF are shown in Figure 16, along with records of the creep rates by other ground-based instruments. We did not find any significant creep signal on the SAF north of the Coachella segment and south of Parkfield. The Creeping segment, covered by dense alignment arrays and other instruments, provides a detailed kinematics of the fault creep [*Brown and Wallace*, 1968; *Burford and Harsh*, 1980; *Burford*, 1988; *Titus et al.*, 2006]. As shown in Figure 16b, we found good agreement between the InSAR observations and the established measurements: creep starts at a "step-over" south of Parkfield and then increases northward. At Parkfield, the creep rate reaches 13 mm/yr. Between Monarch Peak and Parkfield, the creep rates are 25-30 mm/yr, which is compatible with the differential GPS survey by *Titus et al.* [2005] and alignment array surveys by *Burford and Harsh* [1980]. It is noteworthy that north of Monarch Peak (latitudes 36.2-36.4), close to the Smith Ranch (Figure 5b), the creep estimates from InSAR are approximately 20-25 mm/yr, which is lower than the alignment array (AA) surveys of *Burford and Harsh* [1980] by 10 mm/yr.

For creep rates obtained by alignment array method (AA), two different methods should be distinguished. In the study by *Burford and Harsh* [1980], two slip rates (best-fit rates and endpoint rates) are reported from repeated alignment array surveys on the SAF in Central California. The rates from the endpoint method are generally higher than the best-fit rates, sometimes by as large as 10 mm/yr [*Burford and Harsh*, 1980, Table 1]. *Burford and Harsh* [1980] used an example of simple shear distributed across the entire alignment array to justify that the best-fit rates underestimate the amplitude of actual creep. *Titus et al.* [2005] reported two different rates over the Creeping section. They preferred the best-fit rate as a more robust method because it is less sensitive to noise in one single measurement. The best-fit rates reflect the amount of creep within the main slip zone and the endpoint rates probably include auxiliary fractures close to the main slip zone [*Burford and Harsh*, 1980, Figure 2].

At the Smith Ranch site, the endpoint rates from *Burford and Harsh* [1980, Table 1] are 10mm/yr larger than their best-fit rates. *Titus et al.* [2005, 2006] investigated this issue with GPS surveys and they found an average slip rate of 25 mm/yr at the fault, slower than geological slip rate by about 10 mm/yr. Our InSAR-derived creep observation lends further support to their result from GPS. This lower creep rate suggests that over the central segment of the Creeping section the slip rate at the shallow portion of the crust is lower than the slip rate at depth (35 mm/yr) [*Ryder and Burgmann*, 2008; *Rolandone et al.*, 2008].

To the north of the Creeping section, the InSAR-derived creep rates transition gradually to low creep. The creep estimates north of the Bay area are scattered but in general they agree with previous results [*Galehouse and Lienkaemper*, 2003]. As shown in Figure 16, certain estimates of creep rates are negative, which could suggest left-lateral creep or vertical movement across certain faults, however most of these negative rates could reflect negligible surface creep when considering their uncertainties.

Louie et al. [1985] surveyed 3 sites along the Garlock fault with alignment array methods. They found that the site near Cameron on the west Garlock fault experienced a left-lateral creep of >4 mm/yr; two sites on the east Garlock fault exhibited no creep. The InSAR-derived creep estimates supplement the alignment arrays that sparsely sampled the Garlock fault. The LOS direction is more sensitive to the horizontal motion along the east-west trending fault compared to the northwest-southeast trending SAF. As shown in Table 2, we found no significant creep (< 2 mm/yr) along the Garlock fault from InSAR.

The San Jacinto fault is another fault that is not well instrumented with creep measurements. On the northern section of the San Jacinto fault, we found no significant creep (< 2 mm/yr), consistent with alignment array survey at the Clark fault at Anza and the Claremont fault at Colton by *Louie et al.* [1985]. *Louie et al.* [1985] documented aseismic slip on the Coyote Creek fault at Baileys Well with a rate of 5.2 mm/yr since 1971. The

InSAR data shows an average creep rate of 8 mm/yr at the same location, in agreement with previous measurements [*Louie et al.*, 1985].

We computed the difference of the creep rates between InSAR and UCERF2 at the corresponding locations along the SAF and other major faults. We utilize 115 creep data measurements for this comparison, ranging from 0 to 30 mm/yr. Taking the creep rate observations such as creepmeters and alignment arrays to be ground-truth, the overall accuracy of the InSAR-derived creep rates can be evaluated as the standard deviation of the creep rates difference, which is 4.6 mm/yr (Figure 17). The mean absolute deviation, which is less sensitive to outliers, is 3.5 mm/yr. A linear correlation with correlation coefficient of 0.86 is found between the InSAR data and the ground-truth observations.

5.3. Creep rates from the Painted Canyon GPS survey

The surface creep rate at the Southern SAF Coachella segment near Painted Canyon is estimated to be 4-5 mm/yr from InSAR (Figure 16), whereas the rate from alignment arrays and creepmeters for the period of the 1970s to 1980s [*Louie et al.*, 1985] is about 2 mm/yr. It is fortunate that 32 GPS monuments at Painted Canyon were surveyed in February 2007 and February 2010 by geophysicists from UCSD. A. Sylvester from UCSB installed most of the benchmarks in the 1980s for repeated leveling surveys. The 3 year period of separation between the two surveys ensures that the differential displacement across the SAF exceeds the noise level [*Genrich and Bock*, 2006]. As shown in Figure 18, the creep rate is approximately 4.5 mm/yr and there is a 300 m wide deformed zone near the fault trace. No apparent fault-perpendicular velocity or vertical velocity can be distinguished. The excellent agreement between the InSAR and GPS observations validates our assumption that, at least in this area, there is negligible fault-perpendicular motion or vertical motion across the fault when projecting the radar LOS direction into horizontal motion.

This difference between the creep rate from 1970s to 1980s and the creep rate from 2007 to 2010 could be explained by the temporal variation of the surface creep. The geological creep rate [*Sieh and Williams*, 1990] in the past 300 years is 2-4 mm/yr. The dense GPS array at Painted Canyon at almost the same time period of InSAR confirms an accelerated creep rate of 4-5 mm/yr. The non-steadiness of creep on active creeping faults is not a unusual phenomenon and it can be, in general, attributed to a stress perturbation triggered by nearby earthquakes [*Lyons and Sandwell*, 2003]. We suspect that the creep rate from InSAR includes triggered creep from the 2010 El Mayor - Cucapah earthquake.

6. Conclusions

Current interseismic velocity models based on GPS measurements alone cannot resolve features with short wavelengths (<15-40 km). L-band InSAR data is contaminated by errors at longer wavelengths from ionosphere, orbit (plane), and the atmosphere. To remedy these inadequacies, we recovered the interseismic deformation along the entire San Andreas fault at a spatial resolution of 200 meters by combining GPS and InSAR observations using a Sum/Remove/Filter/Restore (SURF) approach. The integration uses a dislocation-based velocity model to interpolate the Line-Of-Sight (LOS) velocity at the full resolution of the InSAR data in radar coordinates. The residual between the model and InSAR LOS velocity were stacked and high-pass filtered, then added back to the model. The filter wavelength is determined by a coherence spectrum analysis of 4 independent interseismic models. Future research should involve a spatially variable crossover wavelength. The LOS velocity data are compared against 1068 GPS velocity measurements. These LOS velocity data and standard deviations are available to modeling groups for future use in their models. We have used these data to systematically estimate fault creep rate along the SAF and 8 major faults and found a general agreement between InSAR and 115 published creep rate measurements. Our next step to advance this work will be to analyze, in detail, the LOS data away from the fault to estimate shallow moment release rate along major segments of the SAF.

Acknowledgments. We thank Matt Wei, Sylvain Barbot, Leah Hogarth, Yariv Hamiel, Diane Rivet, Chris Takeuchi, Danny Brothers, Brent Wheelock, Rob Mellors, Duncan Agnew, Yuri Fialko, Erica Mitchell for their participation in the 2007 and 2010 GPS surveys across the San Andreas fault in Painted Canyon. We thank Yehuda Bock and Brendan Crowell for processing the GPS data from the Painted Canyon survey. The ALOS PALSAR L1.0 data is acquired through Alaska Satellite Facility (ASF). Tom Herring provided the GPS data used to constrain the interseismic velocity model. Duncan Agnew provided the fault traces. This research was supported by the National Science Foundation (EAR 0811772, EAR 0838252, EAR 0847499), NASA (NNX09AD12G), and the SCEC/UCERF-3 program.

References

Baxter, S. C., S. Kedar, J. W. Parker, F. H. Webb, S. E. Owen, A. Sibthorpe, and D. A. Dong (2011), Limitations of strain estimation techniques from discrete deformation observations, *Geophysical Research Letters*, *38*(L01305), doi:10.1029/2010GL046028.

Bird, P. (2009), Long-term fault slip rates, distributed deformation rates, and forecast of seismicity in the western united states from joint fitting of community geologic, geodetic, and stress direction data sets, *Journal of Geophysical Research-Solid Earth*, *114*(B11403), doi:10.1029/2009JB006317.

Brown, R. D. J., and R. E. Wallace (1968), Current and historic fault movement along the san andreas fault between paicines and camp dix, california, in *Conference on Geologic Problems of the San Andreas Fault System*, vol. 11, edited by W. R. Dickinson and A. Grantz, pp. 22–39, Stanford University Publ. Geol. Sci.

Burford, R. O. (1988), Retardations in fault creep rates before local moderate earthquakes along the san-andreas fault system, central california, *Pure and Applied Geophysics*, *126*(2-4), 499–529, doi:10.1007/BF00879008.

Burford, R. O., and P. W. Harsh (1980), Slip on the san-andreas-fault in central california from alignment array surveys, *Bulletin of the Seismological Society of America*, *70*(4), 1233–1261.

Byerlee, J. (1993), Model for episodic flow of high-pressure water in fault zones before earthquakes, *Geology*, *21*(4), 303–306, doi:10.1130/0091-7613.

Chen, C. W., and H. A. Zebker (2000), Network approaches to two-dimensional phase unwrapping: Intractability and two new algorithms, *Journal of the Optical Society of America a-Optics Image Science and Vision*, *17*(3), 401–414, doi:10.1364/JOSAA.17.000401.

Demets, C., R. G. Gordon, D. F. Argus, and S. Stein (1990), Current plate motions, *Geophysical Journal International*, *101*(2), 425–478, doi:10.1111/j.1365-246X.1990.tb06579.x.

Demets, C., R. G. Gordon, D. F. Argus, and S. Stein (1994), Effect of recent revisions to the geomagnetic reversal time-scale on estimates of current plate motions, *Geophysical*

Research Letters, *21*(20), 2191–2194, doi:10.1029/94GL02118.

Emardson, T. R., M. Simons, and F. H. Webb (2003), Neutral atmospheric delay in interferometric synthetic aperture radar applications: Statistical description and mitigation, *Journal of Geophysical Research-Solid Earth*, *108*(B5), doi:10.1029/2002JB001781.

Eneva, M., and D. Adams (2010), Modeling of surface deformation from satellite radar interferometry in the salton sea geothermal field, california, *Geothermal Resources Council Transactions*, *34*, 527–534.

Farr, T. G., P. A. Rosen, E. Caro, R. Crippen, R. Duren, S. Hensley, M. Kobrick, M. Paller, and E. R. et al. (2007), The shuttle radar topography mission, *Reviews of Geophysics*, *45*(2), doi:10.1029/2005RG000183.

Fialko, Y. (2006), Interseismic strain accumulation and the earthquake potential on the southern san andreas fault system, *Nature*, *441*(7096), 968–971, doi:10.1038/nature04797.

Frank, F. C. (1966), Deduction of earth strains from survey data, *Bulletin of the Seismological Society of America*, *56*, 35–42.

Freed, A. M., S. T. Ali, and R. Burgmann (2007), Evolution of stress in southern california for the past 200 years from coseismic, postseismic and interseismic stress changes, *Geophysical Journal International*, *169*(3), 1164–1179, doi:10.1111/j.1365-246X.2007.03391.x.

Galehouse, J. S., and J. J. Lienkaemper (2003), Inferences drawn from two decades of alinement array measurements of creep on faults in the san francisco bay region, *Bulletin of the Seismological Society of America*, *93*(6), 2415–2433, doi:10.1785/0120020226.

Genrich, J. F., and Y. Bock (2006), Instantaneous geodetic positioning with 10-50 hz gps measurements: Noise characteristics and implications for monitoring networks, *Journal of Geophysical Research-Solid Earth*, *111*(B3), doi:10.1029/2005JB003617.

Goldstein, R. M., and C. L. Werner (1998), Radar interferogram filtering for geophysical applications, *Geophysical Research Letters*, *25*(21), 4035–4038, doi:10.1029/1998GL900033.

Gourmelen, N., F. Amelung, and R. Lanari (2010), Interferometric synthetic aperture radar-gps integration: Interseismic strain accumulation across the hunter mountain fault in the eastern california shear zone, *Journal of Geophysical Research-Solid Earth*, *115*(B09408), doi:10.1029/2009JB007064.

Hackl, M., R. Malservisi, and S. Wdowinski (2009), Strain rate patterns from dense gps networks, *Natural Hazards and Earth System Sciences*, *9*(4), 1177–1187.

Hearn, E. H., K. Johnson, and W. Thatcher (2010), Space geodetic data improve seismic hazard assessment in california: Workshop on incorporating geodetic surface deformation data into UCERF3; pomona, california, 12 april 2010, *Eos Trans. AGU*, *91*(38), 336, doi:10.1029/2010EO380007.

Johanson, I. A., and R. Burgmann (2005), Creep and quakes on the northern transition zone of the san andreas fault from gps and insar data, *Geophysical Research Letters*, *32*(14), doi:10.1029/2005GL023150.

Kreemer, C., W. E. Holt, and A. J. Haines (2003), An integrated global model of present-day plate motions and plate boundary deformation, *Geophysical Journal International*, *154*(1), 8–34, doi:10.1046/j.1365-246X.2003.01917.x.

Lienkaemper, J. J., and G. Borchardt (1996), Holocene slip rate of the hayward fault at union city, california, *Journal of Geophysical Research-Solid Earth*, *101*(B3), 6099–6108, doi:10.1029/95JB01378.

Louie, J. N., C. R. Allen, D. C. Johnson, P. C. Haase, and S. N. Cohn (1985), Fault slip in southern-california, *Bulletin of the Seismological Society of America*, *75*(3), 811–833.

Loveless, J. P., and B. J. Meade (2011), Stress modulation on the san andreas fault by interseismic fault system interactions, *Geology*, *39*(11), 1035–1038, doi:10.1130/G32215.1.

Lundgren, P., E. A. Hetland, Z. Liu, and E. J. Fielding (2009), Southern san andreas-san jacinto fault system slip rates estimated from earthquake cycle models constrained by gps and interferometric synthetic aperture radar observations, *Journal of Geophysical Research-Solid Earth*, *114*(B02403), doi:10.1029/2008JB005996.

Lyons, S., and D. Sandwell (2003), Fault creep along the southern san andreas from interferometric synthetic aperture radar, permanent scatterers, and stacking, *Journal of Geophysical Research-Solid Earth*, *108*(B1), doi:10.1029/2002JB001831.

Mccaffrey, R. (2005), Block kinematics of the pacific-north america plate boundary in the southwestern united states from inversion of gps, seismological, and geologic data, *Journal of Geophysical Research-Solid Earth*, *110*(B07401), doi:10.1029/2004jb003307.

Meade, B. J., and B. H. Hager (2005a), Block models of crustal motion in southern california constrained by gps measurements, *Journal of Geophysical Research-Solid Earth*, *110*(B3), doi:10.1029/2004JB003209.

Meade, B. J., and B. H. Hager (2005b), Spatial localization of moment deficits in southern california, *Journal of Geophysical Research-Solid Earth*, *110*(B4), B04,402, doi:10.1029/

2004JB003331.

Molnar, P., and K. E. Dayem (2010), Major intracontinental strike-slip faults and contrasts in lithospheric strength, *Geosphere*, *6*(4), 444–467, doi:10.1130/GES00519.1.

Noriega, G. R., J. R. Arrowsmith, L. B. Grant, and J. J. Young (2006), Stream channel offset and late holocene slip rate of the san andreas fault at the van matre ranch site, carrizo plain, california, *Bulletin of the Seismological Society of America*, *96*(1), 33–47, doi:10.1785/0120050094.

Parsons, T. (2006), Tectonic stressing in california modeled from gps observations, *Journal of Geophysical Research-Solid Earth*, *111*(B3), B03,407, doi:10.1029/2005JB003946.

Peltzer, G., F. Crampe, S. Hensley, and P. Rosen (2001), Transient strain accumulation and fault interaction in the eastern california shear zone, *Geology*, *29*(11), 975–978, doi:10.1130/0091-7613.

Pollitz, F. F., and M. Nyst (2005), A physical model for strain accumulation in the san francisco bay region, *Geophysical Journal International*, *160*(1), 302–317, doi:10.1111/j.1365-246X.2005.02433.x.

Rolandone, F., R. Burgmann, D. C. Agnew, I. A. Johanson, D. C. Templeton, M. A. D'alessio, S. J. Titus, C. Demets, and B. Tikoff (2008), Aseismic slip and fault-normal strain along the central creeping section of the san andreas fault, *Geophysical Research Letters*, *35*(14), doi:10.1029/2008GL034437.

Ryder, I., and R. Burgmann (2008), Spatial variations in slip deficit on the central san andreas fault from insar, *Geophysical Journal International*, *175*(3), 837–852, doi:10.1111/j.1365-246X.2008.03938.x.

Sandwell, D., R. Mellors, X. Tong, M. Wei, and P. Wessel (2011), Open radar interferometry software for mapping surface deformation, *Eos Trans. AGU*, *92*(28), 234, doi:10.1029/2011EO280002.

Sandwell, D. T., and L. Sichoix (2000), Topographic phase recovery from stacked ers interferometry and a low-resolution digital elevation model, *Journal of Geophysical Research-Solid Earth*, *105*(B12), 28,211–28,222.

Savage, J. C., R. W. Simpson, and M. H. Murray (1998), Strain accumulation rates in the san francisco bay area, 1972-1989, *Journal of Geophysical Research-Solid Earth*, *103*(B8), 18,039–18,051, doi:10.1029/98JB01574.

Segall, P. (2002), Integrating geologic and geodetic estimates of slip rate on the san andreas fault system, *International Geology Review*, *44*(1), 62–82, doi:10.2747/0020-6814.44.1.62.

Shen, Z. K., and D. D. Jackson (2005), Southern california tectonic deformation modeling, *Tech. rep.*, Southern California Earthquake Center.

Shen, Z. K., D. D. Jackson, and B. X. Ge (1996), Crustal deformation across and beyond the los angeles basin from geodetic measurements, *Journal of Geophysical Research-Solid Earth*, *101*(B12), 27,957–27,980, doi:10.1029/96JB02544.

Sieh, K. E., and P. L. Williams (1990), Behavior of the southernmost san-andreas fault during the past 300 years, *Journal of Geophysical Research-Solid Earth and Planets*, *95*(B5), 6629–6645, doi:10.1029/JB095iB05p06629.

Smith, B., and D. Sandwell (2003), Coulomb stress accumulation along the san andreas fault system, *Journal of Geophysical Research-Solid Earth*, *108*(B6), doi:10.1029/2002JB002136.

Smith, B., and D. Sandwell (2004), A three-dimensional semianalytic viscoelastic model for time-dependent analyses of the earthquake cycle, *Journal of Geophysical Research-Solid Earth*, *109*(B12), doi:10.1029/2004JB003185.

Smith, B. R., and D. T. Sandwell (2006), A model of the earthquake cycle along the san andreas fault system for the past 1000 years, *Journal of Geophysical Research-Solid Earth*, *111*(B1), B01,405, doi:10.1029/2005JB003703.

Smith-Konter, B., and D. Sandwell (2009), Stress evolution of the san andreas fault system: Recurrence interval versus locking depth, *Geophysical Research Letters*, *36*(L13304), doi:10.1029/2009GL037235.

Sneed, M., and J. T. Brandt (2007), Detection and measurement of land subsidence using global positioning system surveying and interferometric synthetic aperture radar, coachella valley, california, 19962005, *Scientific Investigations Report 20075251, 31 p*, U.S. Geological Survey.

Titus, S. J., C. Demets, and B. Tikoff (2005), New slip rate estimates for the creeping segment of the san andreas fault, california, *Geology*, *33*(3), 205–208, doi:10.1130/G21107.1.

Titus, S. J., C. Demets, and B. Tikoff (2006), Thirty-five-year creep rates for the creeping segment of the san andreas fault and the effects of the 2004 parkfield earthquake: Constraints from alignment arrays, continuous global positioning system, and creepmeters, *Bulletin of the Seismological Society of America*, *96*(4), S250–S268, doi:10.1785/0120050811.

Wei, M., D. Sandwell, and Y. Fialko (2009), A silent m(w) 4.7 slip event of october 2006 on the superstition hills fault, southern california, *Journal of Geophysical Research-Solid*

Earth, *114*, B07,402, doi:10.1029/2008JB006135.

Wei, M., D. Sandwell, and B. Smith-Konter (2010), Optimal combination of insar and gps for measuring interseismic crustal deformation, *Advances in Space Research*, *46*(2), 236–249, doi:10.1016/j.asr.2010.03.013.

Welch, P. D. (1967), The use of fast fourier transform for the estimation of power spectra: A method based on time averaging over short, modified periodograms, *IEEE Transactions on Audio Electroacoustics*, *AU-15*, 7073.

Williams, S., Y. Bock, and P. Fang (1998), Integrated satellite interferometry: Tropospheric noise, gps estimates and implications for interferometric synthetic aperture radar products, *Journal of Geophysical Research-Solid Earth*, *103*(B11), 27,051–27,067, doi:10.1029/98JB02794.

Wisely, B. A., and D. Schmidt (2010), Deciphering vertical deformation and poroelastic parameters in a tectonically active fault-bound aquifer using insar and well level data, san bernardino basin, california, *Geophysical Journal International*, *181*(3), 1185–1200, doi:10.1111/j.1365-246X.2010.04568.x.

Wisely, B. A., D. Schmidt, and R. J. Weldon (2008), Compilation of surface creep on california faults and comparison of wgcep 2007 deformation model to pacific-north american plate motion, appendix p in the uniform california earthquake rupture forecast, version 2 (UCERF 2), *Open File Rep. 2007-1437P*, U.S. Geological Survey.

Zeng, Y., and Z.-K. Shen (2010), A kinematic fault network model of crustal deformation for california and its application to the seismic hazard analysis, *Tech. rep.*, U.S. Geological Survey.

Figure Captions

Figure 1. A map of the San Andreas fault in California in oblique Mercator projection. The gray boxes with track numbers outline the area covered by 13 ALOS ascending tracks. The radar flying direction and look direction are marked. The black lines shows the geological fault traces. Two-character labels with italicized font correspond to major faults mentioned in this paper: MA-Maacama fault, SA-San Andreas fault, RC-Rogers creeks fault, HW-Hayward fault, CF-Calavers fault, RF-Riconada fault, CR-Creeping section, CA-Carrizo segment, GF-Garlock fault, SB-San Bernadino segment, CO-Coachella segment, SJ-San Jacinto fault, EL-Elsnore fault, SH-Superstition hills fault, IM-Imperial fault. Names with regular font are geographic locations: SN-GV-Sierra Nevada Great Valley, LA-Los Angeles basin, MD-Mojave desert, ECSZ-East California shear zone.

Figure 2. Cross comparison of the 4 independent GPS velocity models of the SAF in geographic coordinates. The plots are in Oblique Mercator projection with contour lines in blue. a) Mean of the east component of the velocity models. b) Mean of the north component of the velocity models. c) Standard deviation of the east component of the velocity models. d) Standard deviation of the north component of the velocity models. The contours are at 2.5 mm/yr interval for a) and b) and at 0.5 mm/yr interval for c) and d). The black lines show the geological fault traces.

Figure 3. a) The 37 transect lines (solid lines and dashed lines) show the profiles used in the coherence spectrum analysis. The 18 solid transect lines show the profiles used

in the power spectrum analysis (Figure 15). b) Coherence as a function of wavenumber for 4 independent GPS-derived models. The coherence spectrum for 6 pairs of the GPS velocity models are compared here: H-model from *Meade and Hager* [2005a]; M-model from *Mccaffrey* [2005]; Z-model from *Zeng and Shen* [2010]; S-model from *Smith-Konter and Sandwell* [2009]. c) Average of the 6 pairs of coherence spectrum.

Figure 4. Crustal velocity model in line-of-sight (LOS) velocity based on regional the GPS velocity field [*Smith-Konter and Sandwell*, 2009] in oblique Mercator projection. The colors represent the LOS velocity field along 13 ALOS ascending tracks represented by radar swaths (Figure 1). Positive velocities (reds) show the ground moving relatively away from the satellite (81° azimuth, 37° from vertical). The small triangles are the GPS stations used to constrain the velocity model. The black lines shows the geological fault traces.

Figure 5. a) Interseismic deformation of the SAF derived from integrating the GPS observations with ALOS radar interferograms (2006.5-2010). Positive velocities (reds) show the ground moving away from the satellite (81° azimuth, 37° from vertical). The shading highlights the gradient in the velocity field. The areas with low coherence and large standard deviation (¿ 6 mm/yr) are masked. GPS sites are shown as triangles. b) Southern part of the SAFS shows the broad transition in velocity across the San Andreas and San Jacinto. c) Central section of the SAFS shows the sharp velocity gradient across the Creeping Section. The black star marks the location of the Smith Ranch. The black boxes mark the locations of the velocity profiles shown in Figure 12. A full

resolution version of this LOS velocity map and its relationship to faults and cultural features can be downloaded as a KML-file for Google Earth from the following site: `ftp://topex.ucsd.edu/pub/SAF_models/insar/ALOS_ASC_masked.kmz`

Figure 6. Example perpendicular baseline vs. time plot showing the “leap-frog” alignment approach taken prior to forming the interferograms. The track number is 212 and the orbital indices are shown as 5-digits number in the plot. Image 10024 is boxed, representing the super master image. Primary matches (those that plot close to the super master in the baseline-time domain) are represented by blue dots. Secondary matches are represented by red dots.

Figure 7. Example perpendicular baseline vs. time plot showing interferometric pairs used in the stacking. The track number is 212 and the orbital indices are shown as 5-digit numbers in the plot.

Figure 8. Flowchart for iterative phase unwapping of a single interferogram.

Figure 9. Flowchart of combining InSAR stacks with GPS observations [*Wei et al.*, 2010]

Figure 10. High-pass filtered residual velocity (2006.5-2010) along ALOS ascending tracks.

Figure 11. Standard deviation of the average LOS velocity (2006.5-2010) along ALOS ascending tracks.

Figure 12. Averaged LOS velocity profiles perpendicular to the fault over Central California along the Creeping section of the SAF (Figure 5c). The blue dots with 1-standard deviation errors bars indicate the total LOS velocity and the black lines are the GPS model. a) Profile taken along the northern segment of the Creeping section. b) Profile taken along the central segment of the Creeping section. c) Profile taken along the southern segment of the Creeping section.

Figure 13. Comparison between the InSAR LOS velocity and the GPS observations projected into LOS coordinates. a) and b): histogram of $V_{diff}(x) = V_{GPS}(x) - V_{InSAR}(x)$ for 1068 GPS sites. c) and d): $V_{InSAR}(x)$ against $V_{GPS}(x)$. e) and f): comparison of the standard deviations and . Both the vertical and the horizontal components of the GPS velocity are used in the projection for a), c), and e). Only the horizontal components of the GPS velocity are used in the projection for b), d), and f).

Figure 14. The standard deviations of $V_{diff}(x) = V_{GPS}(x) - V_{InSAR}(x)$ as a function of spatial averaging. std means the standard deviations and mad means the median absolute deviations. The horizontal axis is in arcminutes. One arcminute is approximately 2 km in distance. In the legend, 3-components represents both horizontal and vertical displacements while 2-components represents horizontal displacements only.

Figure 15. a) Power spectrum of the GPS model and the InSAR LOS velocity data with their power law fitting curves. b) Coherence spectrum between GPS model and the InSAR LOS velocity data.

Figure 16. Creep rate comparison with an independent data set compiled by UCERF2. The red circles are the creep rate from InSAR in the period from 2006.5 to 2010 (this study). The error bars show the 1σ (σ is the standard deviation) uncertainty. The triangles and other symbols are independent creep measurements compiled by UCERF2. AA means alignment array; CM means creep meters; Cult means cultural offset. a) Creep rate along the entire SAF from north to south. The inset on the upper right corner shows the linear regression method to determine the surface creep rate across fault. b) A zoomed-in view at the Creeping section in Central California. See text for details.

Figure 17. Creep rates estimates from InSAR and from ground-based instruments compiled by UCERF2 (alignment arrays, GPS, creepmeters, cultural offsets). a) Histogram of the creep rates difference between InSAR and UCERF2 creep rate datasets. b) Scatter plot of the creep rate data from InSAR versus UCERF2.

Figure 18. Campaign GPS survey at Paint Canyon at 2007 and 2010. The vectors in the top subplot show the horizontal GPS velocity, with 95% confidence ellipses. The black dots mark the SAF. The background is the recovered high-resolution LOS velocity map. Two base stations PAIN and SABR are labeled. The 3 bottom subplots show the fault parallel velocity, fault perpendicular velocity and vertical velocity, respectively, across the

fault trace.

Table 1: Data information about ALOS ascending tracks.

Track	Frame	Sum of perpendicular baseline (m)	Number of interferograms	Total time span (days)
224	780	-16	28	22724
224	770	-16	28	22724
224	760	-82	26	20930
223	750	148	16	14674
223	760	148	16	14674
223	770	148	16	14674
223	780	148	16	14674
222	780	-146	23	18676
222	770	-146	23	18676
222	760	-146	23	18676
222	750	-146	23	18676
222	740	-146	23	18676
222	730	-146	23	18676
222	720	9	19	17250
222	710	9	19	17250
221	710	-34	15	12374
221	720	30	8	7314
221	730	-104	14	11362
221	740	-104	14	11362
220	700	32	14	13110
220	710	32	14	13110
220	720	32	14	13110
219	690	13	29	24932
219	700	13	29	24932
218	670	3	23	19090
218	680	3	23	19090
218	690	3	23	19090
217	670	15	13	11914
217	680	15	13	11914
217	690	15	13	11914
216	660	7	24	20838
216	670	7	24	20838
216	680	-60	23	19826
216	690	-60	23	19826
215	650	-65	9	6900
215	660	-6	11	9200
215	670	-6	11	9200
215	680	-6	11	9200
215	690	-104	16	13708
215	700	-104	16	13708
214	650	1	21	18952
214	660	1	21	18952

Table 1 – Continued

Track	Frame	Sum of perpendicular baseline (m)	Number of interferograms	Total time span (days)
214	670	1	21	18952
214	680	1	21	18952
214	690	1	21	18952
214	700	1	21	18952
213	650	-228	33	28428
213	660	-228	33	28428
213	670	-228	33	28428
213	680	-228	33	28428
213	690	-228	33	28428
213	700	-228	33	28428
212	650	-1	10	9384
212	660	-1	10	9384
212	670	-1	10	9384
212	680	-1	10	9384
212	690	-151	9	8418
212	700	-151	9	8418

Table 2: Creep rate on San Andreas fault system.

San Andreas Fault

Latitude (degrees)	Longitude (degrees)	Creep rate[a] (mm/yr)	Creep rate uncertainty (mm/yr)	Scale[b]
33.349	-115.724	0.025	0.730	3.163
33.416	-115.799	4.074	0.629	2.643
33.475	-115.877	0.018	1.242	2.698
33.542	-115.951	4.299	0.802	3.075
33.608	-116.026	4.076	0.241	2.695
33.669	-116.102	4.762	0.642	2.902
33.734	-116.178	4.005	1.110	2.822
33.796	-116.255	0.139	0.138	2.666
33.856	-116.336	0.876	0.298	2.526
33.907	-116.422	0.939	0.396	2.360
33.962	-116.508	-0.618	0.410	2.475
34.013	-116.600	-0.598	0.393	1.938
34.042	-116.701	0.624	0.691	1.825
34.063	-116.806	1.089	1.413	1.772
34.078	-116.912	2.020	1.637	1.783
34.101	-117.017	-0.404	1.915	1.821
34.124	-117.121	0.081	0.537	1.845
34.151	-117.223	0.013	0.326	1.933
34.194	-117.319	0.346	0.505	2.175
34.245	-117.411	0.116	0.590	2.230

Table 2 – Continued

Latitude (degrees)	Longitude (degrees)	Creep rate[a] (mm/yr)	Creep rate uncertainty (mm/yr)	Scale[b]
34.292	-117.503	-1.904	1.885	2.230
34.339	-117.597	-5.121	5.177	2.125
34.378	-117.694	-1.187	1.673	2.038
34.418	-117.791	-2.074	0.611	2.039
34.457	-117.888	-0.901	0.103	2.058
34.498	-117.985	0.056	0.241	2.059
34.539	-118.082	-1.640	0.509	2.059
34.578	-118.181	-0.798	0.304	2.001
34.616	-118.280	-1.602	0.884	1.983
34.652	-118.379	-1.176	1.137	1.984
34.688	-118.480	-5.093	0.956	1.920
34.719	-118.582	-2.272	1.089	1.888
34.749	-118.685	-0.701	0.982	1.888
34.777	-118.789	-1.425	0.675	1.862
34.808	-118.893	-1.755	0.681	1.919
34.824	-118.998	-1.012	0.345	1.730
34.846	-119.105	1.344	0.444	1.775
34.860	-119.211	0.298	0.413	1.868
34.895	-119.312	2.101	0.872	1.999
34.941	-119.405	-0.850	0.765	2.456
34.998	-119.492	-1.631	0.274	2.490
35.057	-119.575	-1.647	0.844	2.770
35.120	-119.655	-0.175	0.565	2.732
35.183	-119.732	0.602	1.220	3.020
35.250	-119.805	0.016	2.546	3.188
35.319	-119.877	0.609	0.857	3.199
35.387	-119.946	0.800	0.885	3.298
35.461	-120.013	-0.593	2.139	3.627
35.531	-120.081	0.338	0.987	3.361
35.600	-120.152	-4.464	0.845	3.052
35.667	-120.224	1.856	0.522	3.355
35.738	-120.294	2.143	0.963	3.357
35.823	-120.355	-5.286	3.173	3.086
35.880	-120.418	14.159	1.672	3.087
35.948	-120.493	26.732	1.783	3.056
36.011	-120.569	30.670	3.531	2.974
36.077	-120.645	26.096	2.101	2.853
36.146	-120.719	28.821	3.810	3.201
36.206	-120.790	19.429	3.770	2.902
36.280	-120.862	24.352	1.965	2.997
36.346	-120.935	18.891	1.152	3.119
36.419	-121.006	20.710	3.553	3.423

Table 2 – Continued

Latitude (degrees)	Longitude (degrees)	Creep rate[a] (mm/yr)	Creep rate uncertainty (mm/yr)	Scale[b]
36.489	-121.077	22.461	2.733	3.167
36.556	-121.149	23.446	2.106	3.167
36.623	-121.223	11.006	1.550	2.955
36.689	-121.301	7.194	3.438	2.695
36.748	-121.384	15.479	1.590	2.402
36.802	-121.471	10.286	1.826	2.465
36.862	-121.557	4.543	2.084	2.722
36.919	-121.642	2.192	0.524	2.521
36.981	-121.724	0.343	1.174	2.871
37.098	-121.891	-1.910	1.456	2.315
37.160	-121.975	-4.693	2.182	2.799
37.357	-122.206	-2.632	3.124	3.481
37.500	-122.342	-3.671	5.213	3.898
37.877	-122.651	3.793	3.884	3.893
37.951	-122.715	-1.183	2.809	3.896
38.098	-122.846	9.042	5.003	3.696
38.319	-123.041	0.751	2.882	4.285
38.532	-123.250	1.216	2.051	3.292
38.603	-123.322	-4.390	1.316	3.425
38.673	-123.392	-8.293	3.702	3.428
38.743	-123.462	-8.131	2.212	3.431
38.817	-123.530	0.242	1.453	3.866
38.892	-123.596	-1.140	2.282	3.870
38.965	-123.661	-3.385	3.239	3.874

Maacama fault

Latitude (degrees)	Longitude (degrees)	Creep rate[a] (mm/yr)	Creep rate uncertainty (mm/yr)	Scale[b]
38.786	-122.922	4.794	1.988	3.053
38.859	-122.993	-1.683	1.067	3.885
38.937	-123.048	8.481	5.452	5.635
39.018	-123.095	2.445	1.547	6.362
39.100	-123.143	2.749	1.301	6.372
39.181	-123.191	3.014	1.027	4.837
39.260	-123.248	-7.650	2.828	4.842
39.339	-123.305	0.846	2.700	4.848
39.420	-123.353	-6.367	6.170	6.319
39.502	-123.401	-8.432	6.456	6.085
39.584	-123.451	-13.417	3.456	6.091
39.665	-123.502	0.200	1.696	5.145

Table 2 – Continued

Latitude (degrees)	Longitude (degrees)	Creep rate[a] (mm/yr)	Creep rate uncertainty (mm/yr)	Scale[b]
39.744	-123.557	-0.966	1.532	5.152

Bartlett Springs fault

Latitude (degrees)	Longitude (degrees)	Creep rate[a] (mm/yr)	Creep rate uncertainty (mm/yr)	Scale[b]
39.038	-122.532	0.517	0.962	3.828
39.107	-122.623	1.776	1.369	3.270
39.170	-122.692	-4.980	2.055	2.443
39.234	-122.768	0.268	0.930	3.150
39.304	-122.833	-0.428	1.171	4.821
39.378	-122.899	-2.381	1.950	4.206
39.454	-122.959	-0.123	2.040	4.030
39.533	-123.020	6.946	4.026	5.388

Concord fault

Latitude (degrees)	Longitude (degrees)	Creep rate[a] (mm/yr)	Creep rate uncertainty (mm/yr)	Scale[b]
37.972	-122.036	1.738	1.550	5.099

Rogers Creek fault

Latitude (degrees)	Longitude (degrees)	Creep rate[a] (mm/yr)	Creep rate uncertainty (mm/yr)	Scale[b]
38.170	-122.449	3.851	3.335	3.386
38.242	-122.520	-2.919	1.955	3.453
38.313	-122.594	-3.240	1.706	4.138
38.387	-122.654	2.083	2.017	4.204
38.465	-122.712	3.222	1.252	5.663

Calaveras fault

Latitude (degrees)	Longitude (degrees)	Creep rate[a] (mm/yr)	Creep rate uncertainty (mm/yr)	Scale[b]
36.628	-121.189	7.420	2.063	3.053
36.697	-121.266	-0.533	1.552	3.214
36.766	-121.339	0.427	1.598	3.217
36.842	-121.396	5.190	2.051	5.806
36.924	-121.436	8.880	11.067	7.177
37.005	-121.483	7.157	2.284	4.660

Table 2 – Continued

Latitude (degrees)	Longitude (degrees)	Creep rate[a] (mm/yr)	Creep rate uncertainty (mm/yr)	Scale[b]
37.084	-121.538	25.304	2.426	4.960
37.161	-121.598	9.220	1.458	3.971
37.238	-121.656	-3.419	1.843	4.612
37.315	-121.712	-3.855	4.634	4.617
37.392	-121.768	4.576	1.833	4.675
37.473	-121.819	-4.378	5.807	7.642
37.557	-121.859	14.671	6.272	11.950
37.640	-121.902	-2.585	2.477	5.413
37.721	-121.945	4.922	1.950	6.041

Hayward fault

Latitude (degrees)	Longitude (degrees)	Creep rate[a] (mm/yr)	Creep rate uncertainty (mm/yr)	Scale[b]
37.526	-121.949	5.708	1.137	3.943
37.601	-122.012	2.505	0.946	3.425
37.673	-122.083	2.907	0.528	3.439
37.746	-122.143	1.291	0.586	3.557
37.821	-122.210	3.554	0.297	4.144
37.896	-122.270	4.910	0.718	4.243

Garlock fault

Latitude (degrees)	Longitude (degrees)	Creep rate[a] (mm/yr)	Creep rate uncertainty (mm/yr)	Scale[b]
34.826	-118.867	0.448	0.532	1.821
34.881	-118.771	0.954	0.543	1.846
34.924	-118.676	0.366	0.572	1.746
34.965	-118.578	-0.619	0.305	1.711
34.995	-118.479	1.717	0.609	1.780
35.044	-118.386	-0.349	0.477	1.917
35.098	-118.296	-1.688	0.419	1.839
35.145	-118.203	0.518	0.261	1.850
35.190	-118.112	-0.025	0.077	1.871
35.246	-118.025	0.073	0.593	1.902
35.309	-117.944	-2.065	2.262	2.047
35.368	-117.860	0.255	1.099	1.829
35.412	-117.766	0.042	0.255	1.774
35.449	-117.665	0.548	0.150	1.705
35.477	-117.561	0.467	0.252	1.683
35.504	-117.456	-0.320	0.055	1.669
35.526	-117.349	0.302	0.187	1.675

Table 2 – Continued

Latitude (degrees)	Longitude (degrees)	Creep rate[a] (mm/yr)	Creep rate uncertainty (mm/yr)	Scale[b]
35.551	-117.242	1.583	0.219	1.675
35.575	-117.136	0.516	0.190	1.675
35.595	-117.029	-0.702	0.210	1.666
35.604	-116.920	-0.360	0.097	1.665
35.596	-116.810	-0.088	0.091	1.665
35.593	-116.700	-0.869	0.483	1.682
35.591	-116.590	0.068	0.092	1.669

San Jacinto fault

Latitude (degrees)	Longitude (degrees)	Creep rate[a] (mm/yr)	Creep rate uncertainty (mm/yr)	Scale[b]
33.033	-116.004	-1.629	1.614	2.898
33.099	-116.056	8.579	0.896	3.938
33.164	-116.143	2.212	1.180	2.675
33.222	-116.217	0.186	0.398	2.442
33.282	-116.296	-2.118	0.745	2.975
33.346	-116.371	-0.184	0.806	2.751
33.407	-116.453	-0.659	0.260	2.648
33.473	-116.516	-1.115	0.675	5.928
33.538	-116.588	0.709	0.569	2.872
33.594	-116.679	0.317	1.258	2.434
33.647	-116.763	1.189	1.053	2.255
33.698	-116.855	0.806	1.565	2.279
33.753	-116.952	2.230	1.063	2.280
33.815	-116.966	-12.948	2.936	2.496
33.877	-117.055	0.362	3.404	2.671
33.938	-117.135	-5.653	1.462	2.733
34.001	-117.215	1.442	0.678	2.946
34.067	-117.287	0.610	0.690	3.272
34.135	-117.358	6.505	2.733	3.274
34.198	-117.424	-0.316	2.192	2.417
34.253	-117.518	-0.875	2.281	2.283
34.311	-117.602	-0.308	1.204	2.594

Superstition fault

Latitude (degrees)	Longitude (degrees)	Creep rate[a] (mm/yr)	Creep rate uncertainty (mm/yr)	Scale[b]
32.923	-115.692	1.066	2.930	2.731
32.984	-115.769	2.786	0.400	2.478

Table 2 – Continued

Latitude (degrees)	Longitude (degrees)	Creep rate[a] (mm/yr)	Creep rate uncertainty (mm/yr)	Scale[b]

[a] Positive creep rate implies right-lateral slip; negative creep rate implies left-lateral slip.

[b] Scale is a factor that used to convert LOS to horizontal velocity.

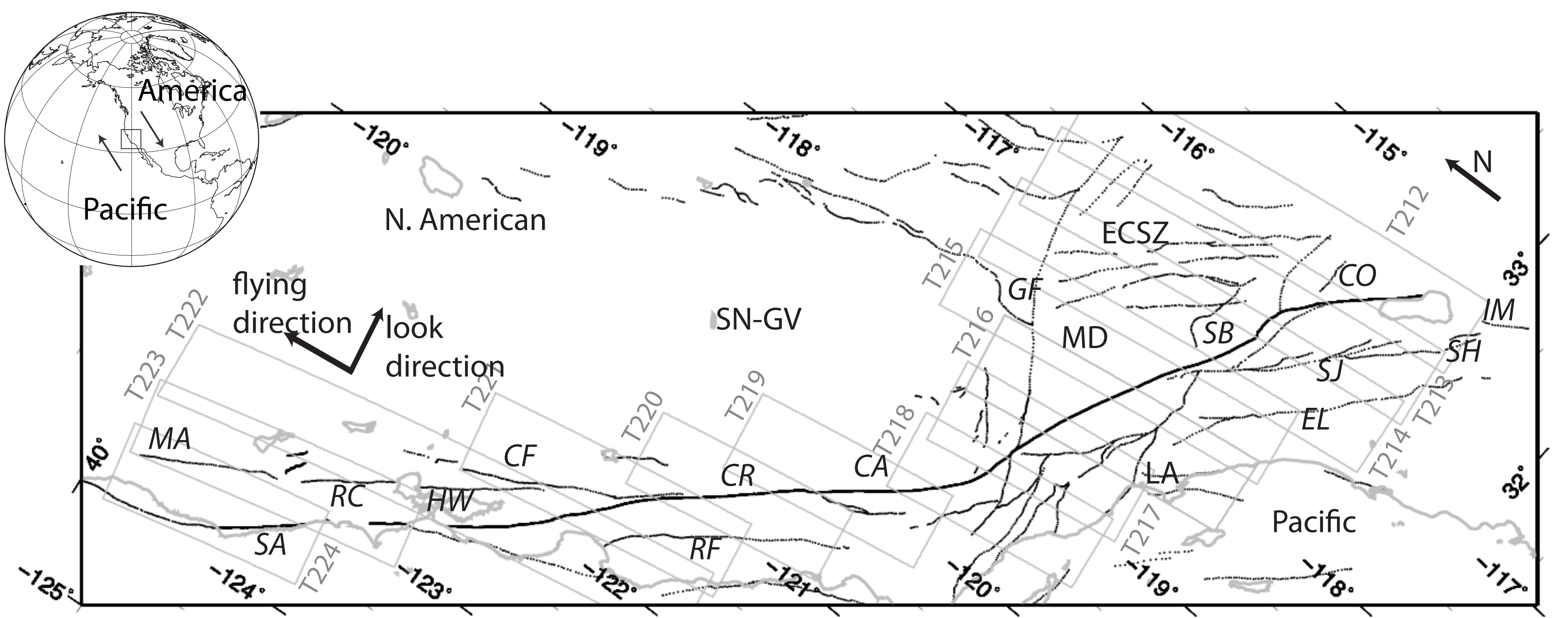

America
Pacific
N. American
SN-GV
ECSZ
N
flying direction
look direction
GF
MD
CO
SB
IM
SH
SJ
EL
LA
Pacific
MA
RC
HW
SA
CF
CR
RF
CA
T212
T213
T214
T215
T216
T217
T218
T219
T220
T221
T222
T223
T224
−125°
−124°
−123°
−122°
−121°
−120°
−119°
−118°
−117°
−116°
−115°
40°
33°
32°

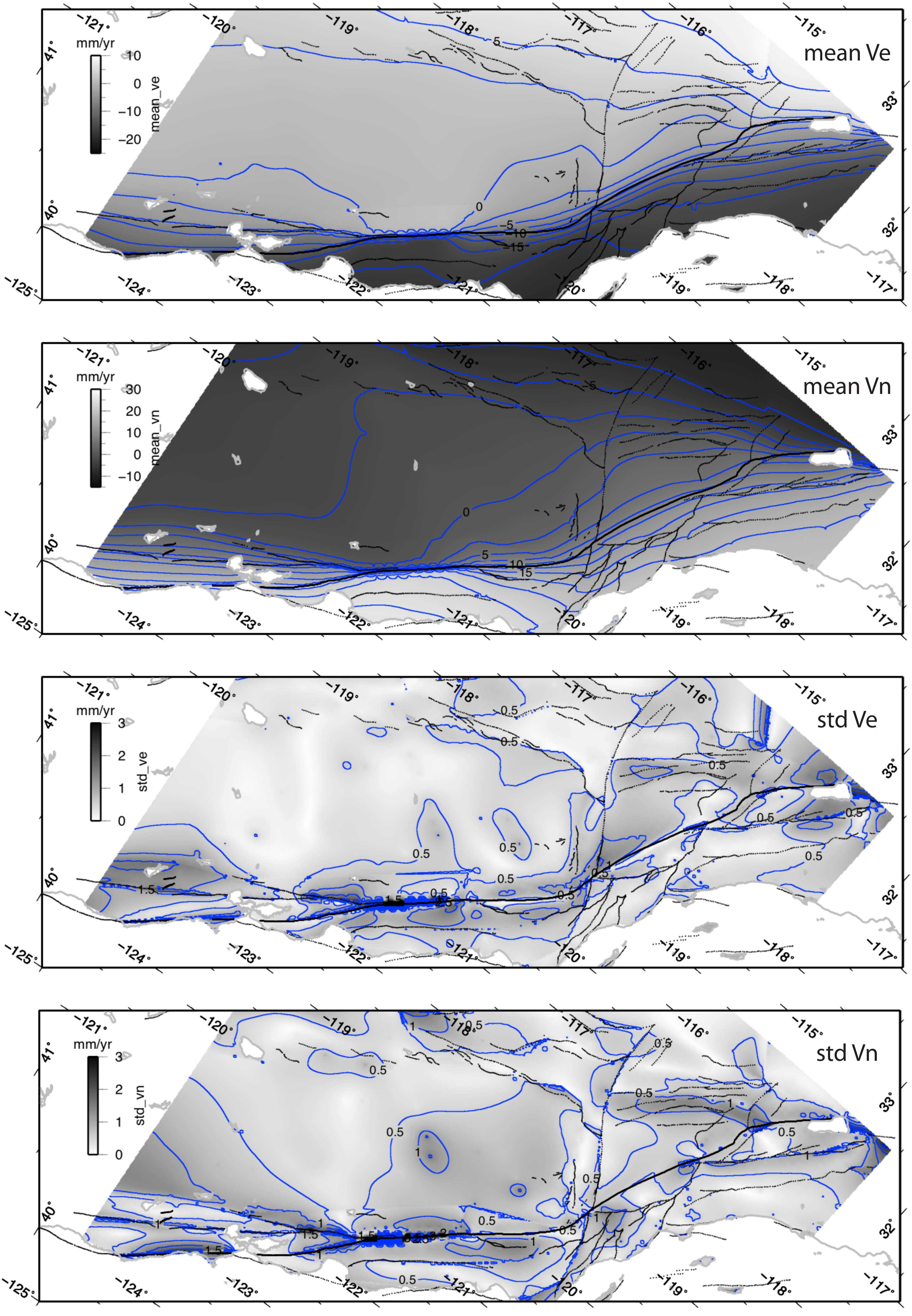

mean Ve
mm/yr
mean_ve
10
0
−10
−20
mean Vn
mm/yr
mean_vn
30
20
10
0
−10
std Ve
mm/yr
std_ve
3
2
1
0
std Vn
mm/yr
std_vn
3
2
1
0

a) location of the transects used in this spectrum analysis

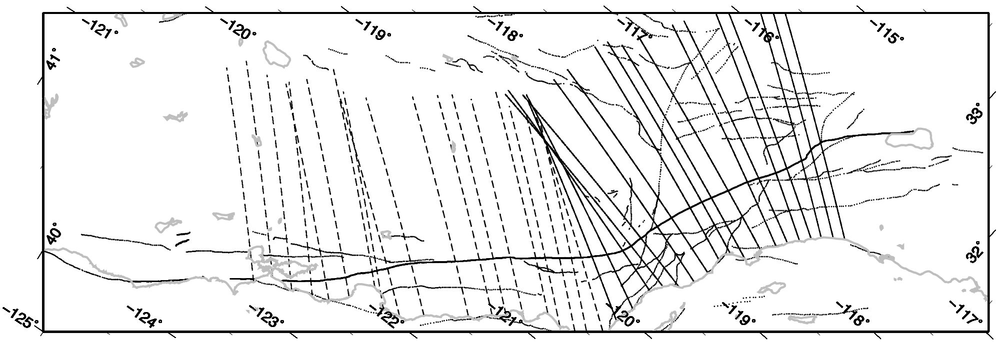

b) coherence spectrum for 6 pairs of GPS model

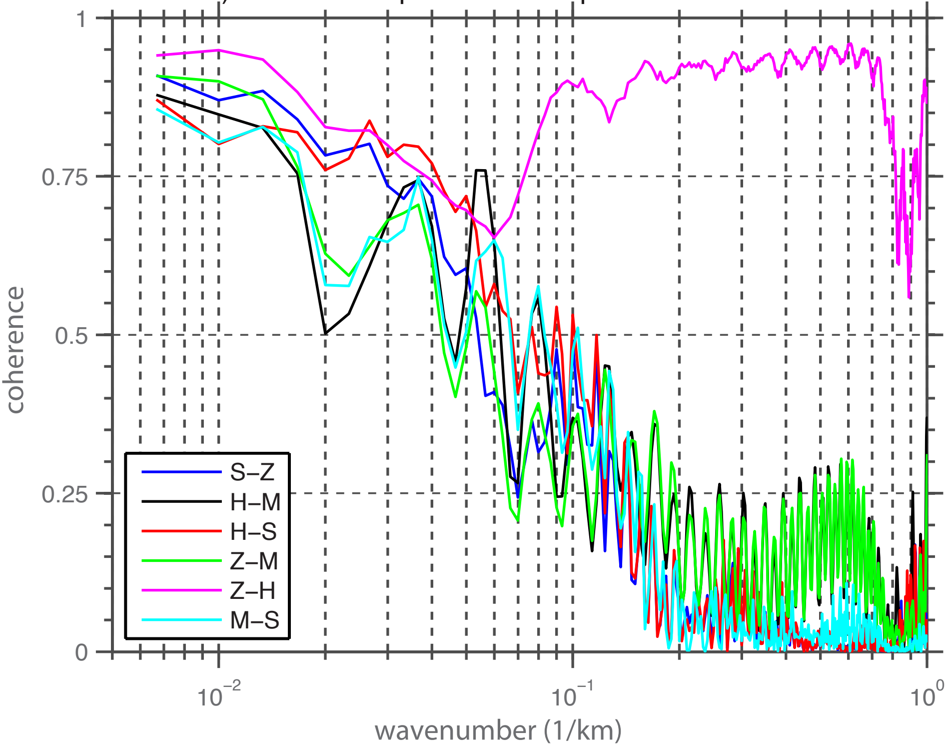

c) averaged coherence spectrum

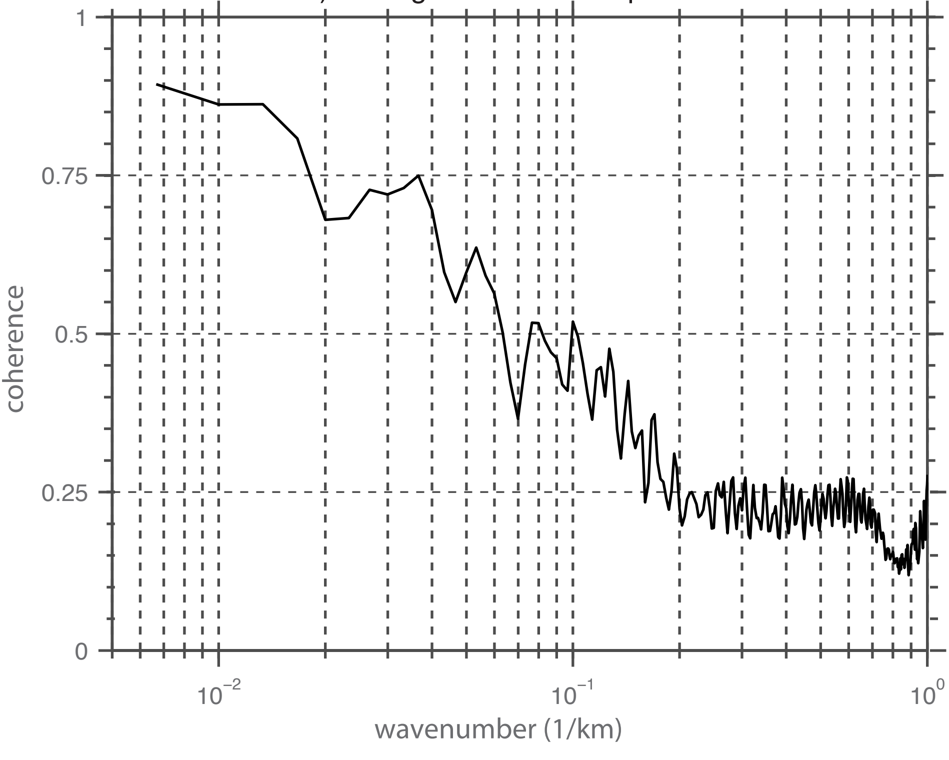

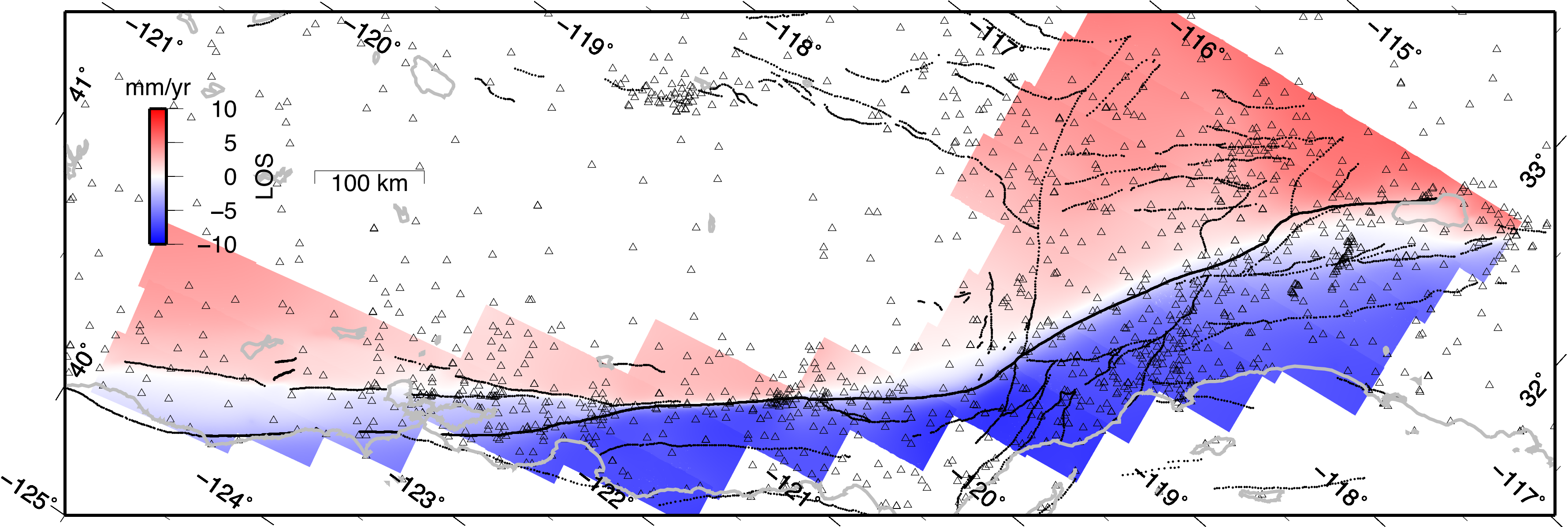

mm/yr
10
5
0
−5
−10
LOS
100 km
−121°
−120°
−119°
−118°
−117°
−116°
−115°
41°
40°
33°
32°
−125°
−124°
−123°
−122°
−121°
−120°
−119°
−118°
−117°

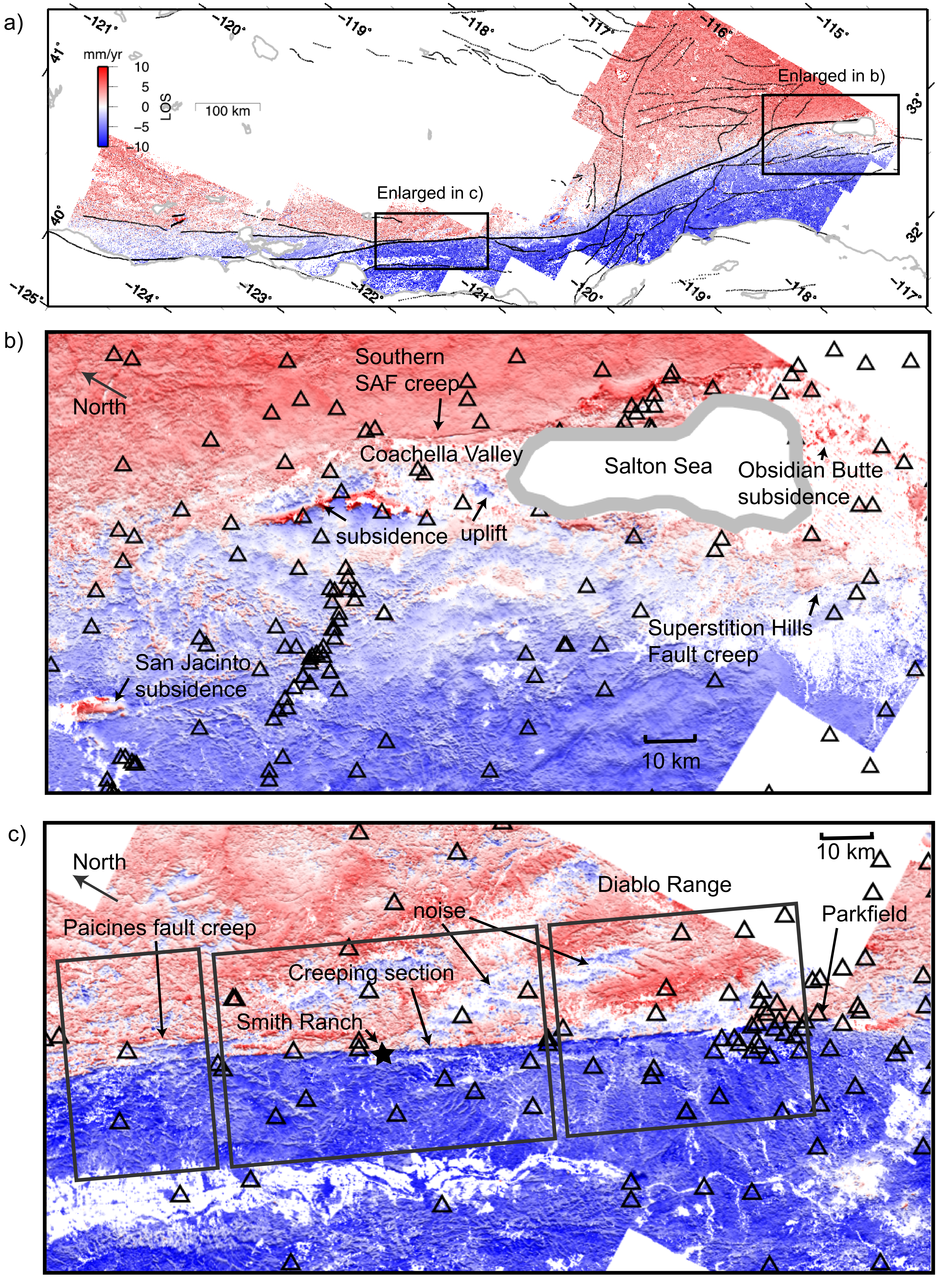
a)
mm/yr
10
5
0
−5
−10
LOS
100 km
Enlarged in b)
Enlarged in c)
−121° −120° −119° −118° −117° −116° −115°
−125° −124° −123° −122° −121° −120° −119° −118° −117°
41° 40° 33° 32°
b)
North
Southern SAF creep
Coachella Valley
Salton Sea
Obsidian Butte subsidence
subsidence
uplift
San Jacinto subsidence
Superstition Hills Fault creep
10 km
c)
North
10 km
Diablo Range
Parkfield
noise
Paicines fault creep
Creeping section
Smith Ranch

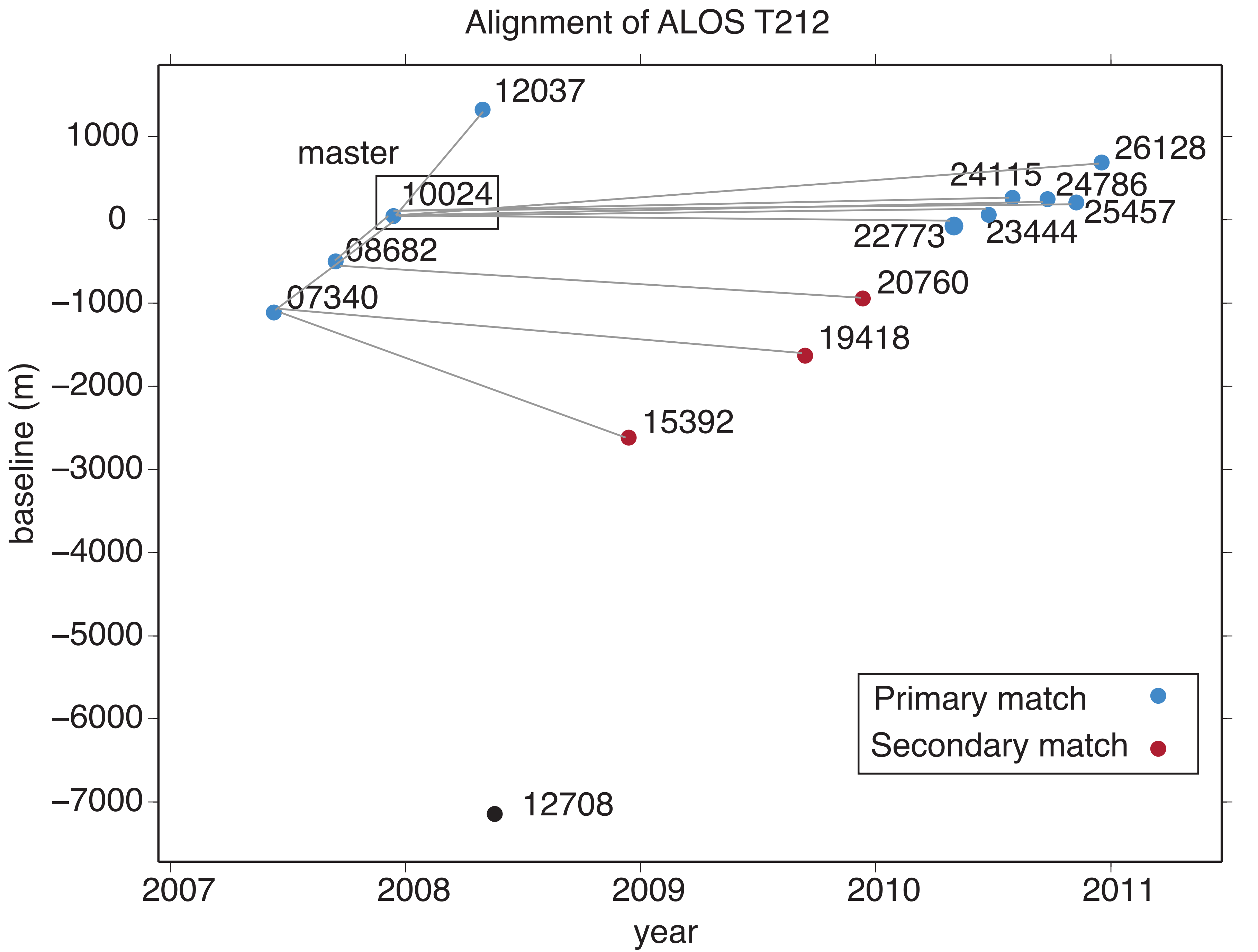

Alignment of ALOS T212
baseline (m)
year
master
12037
10024
08682
07340
26128
24115
24786
25457
22773
23444
20760
19418
15392
12708
Primary match
Secondary match
1000
0
−1000
−2000
−3000
−4000
−5000
−6000
−7000
2007
2008
2009
2010
2011

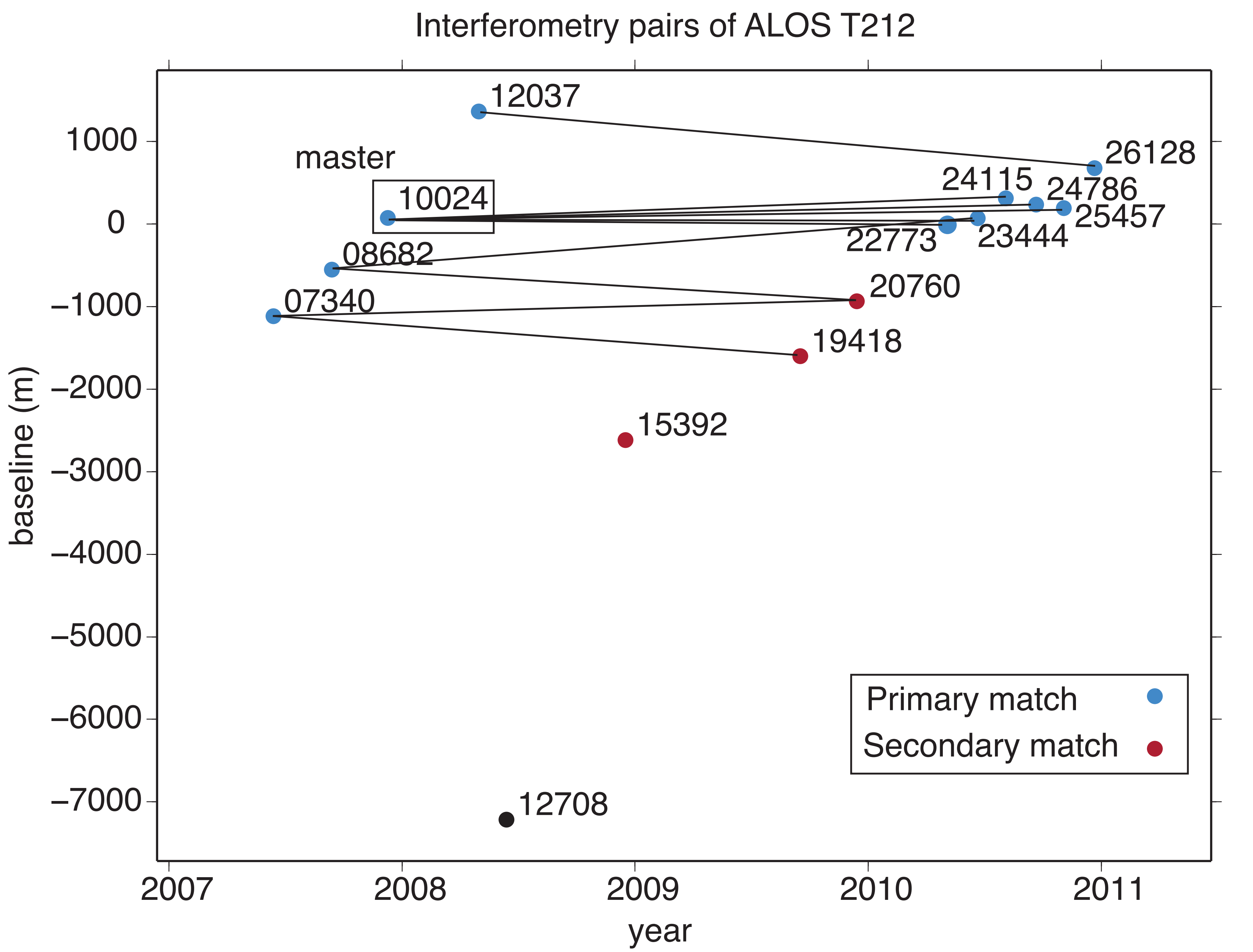
Interferometry pairs of ALOS T212
master
10024
12037
26128
24115
24786
25457
22773
23444
08682
20760
07340
19418
15392
12708
1000
0
−1000
−2000
−3000
−4000
−5000
−6000
−7000
baseline (m)
2007
2008
2009
2010
2011
year
Primary match
Secondary match

Flowchart of processing an interferogram

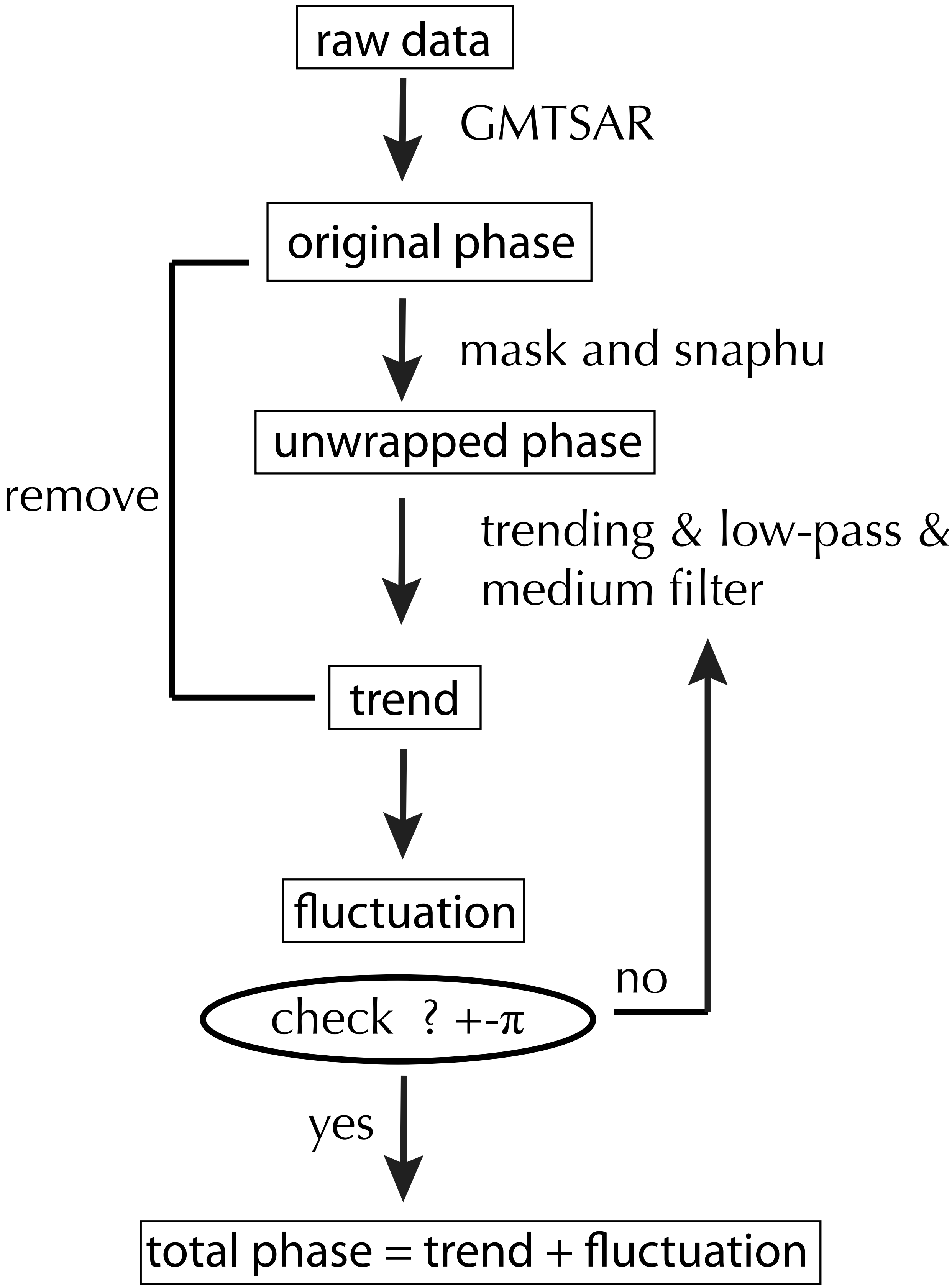

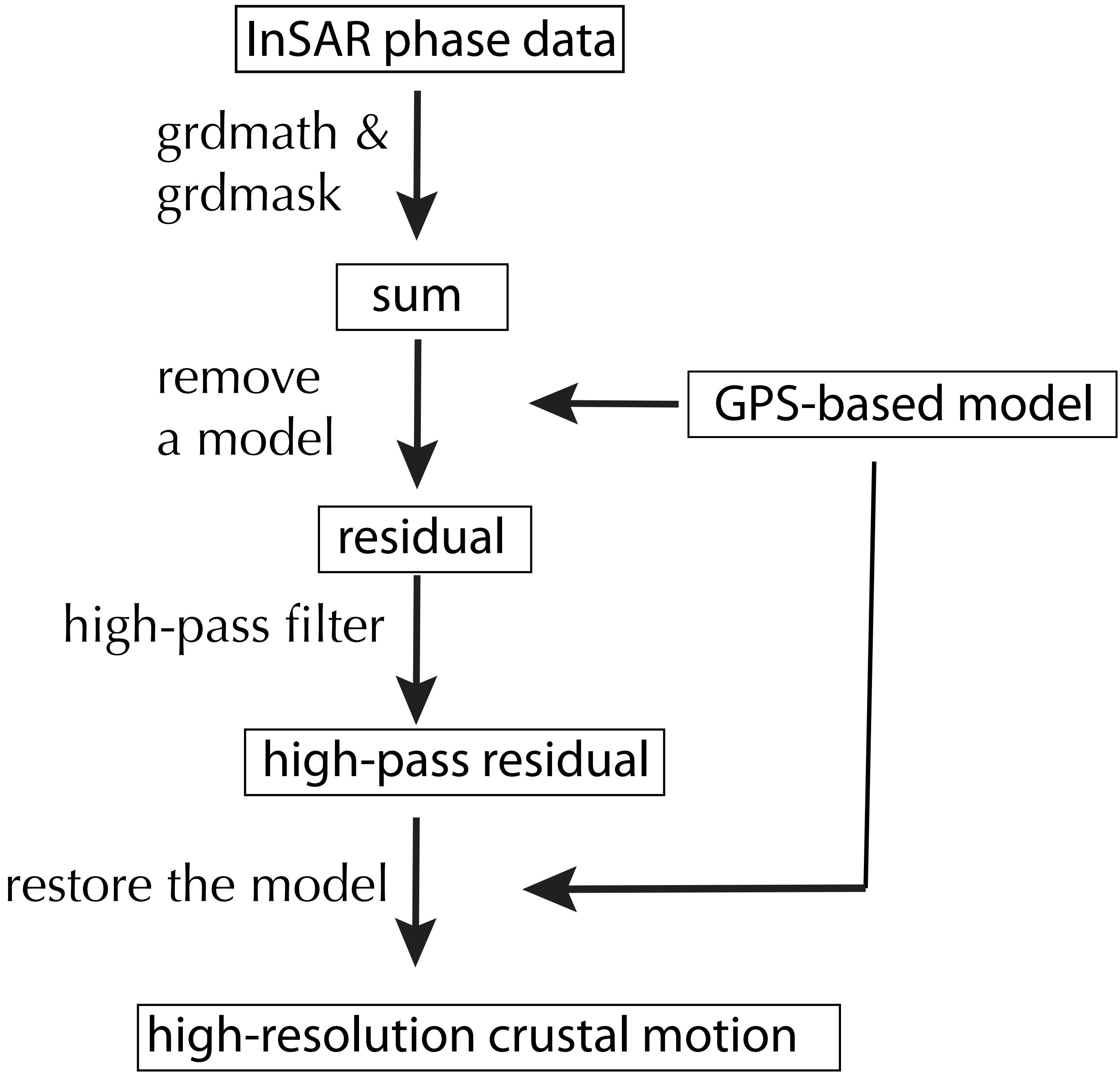
InSAR phase data
grdmath &
grdmask
sum
remove
a model
GPS-based model
residual
high-pass filter
high-pass residual
restore the model
high-resolution crustal motion

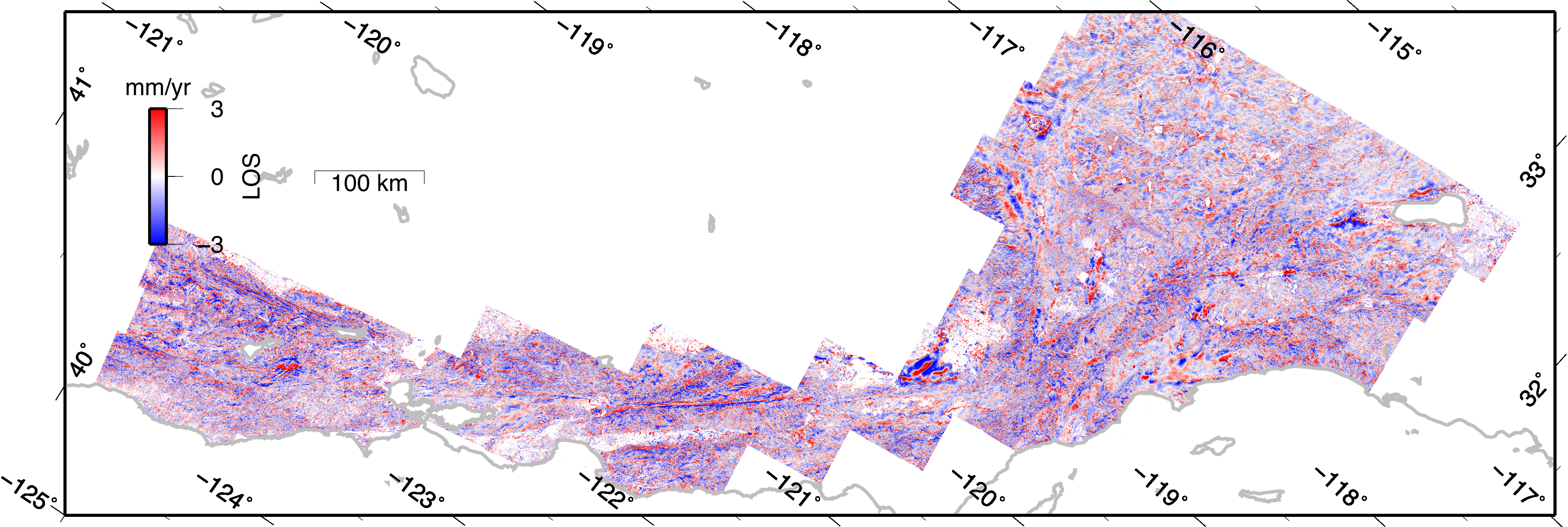
mm/yr
3
0
−3
LOS
100 km
−121°
−120°
−119°
−118°
−117°
−116°
−115°
41°
40°
33°
32°
−125°
−124°
−123°
−122°
−121°
−120°
−119°
−118°
−117°

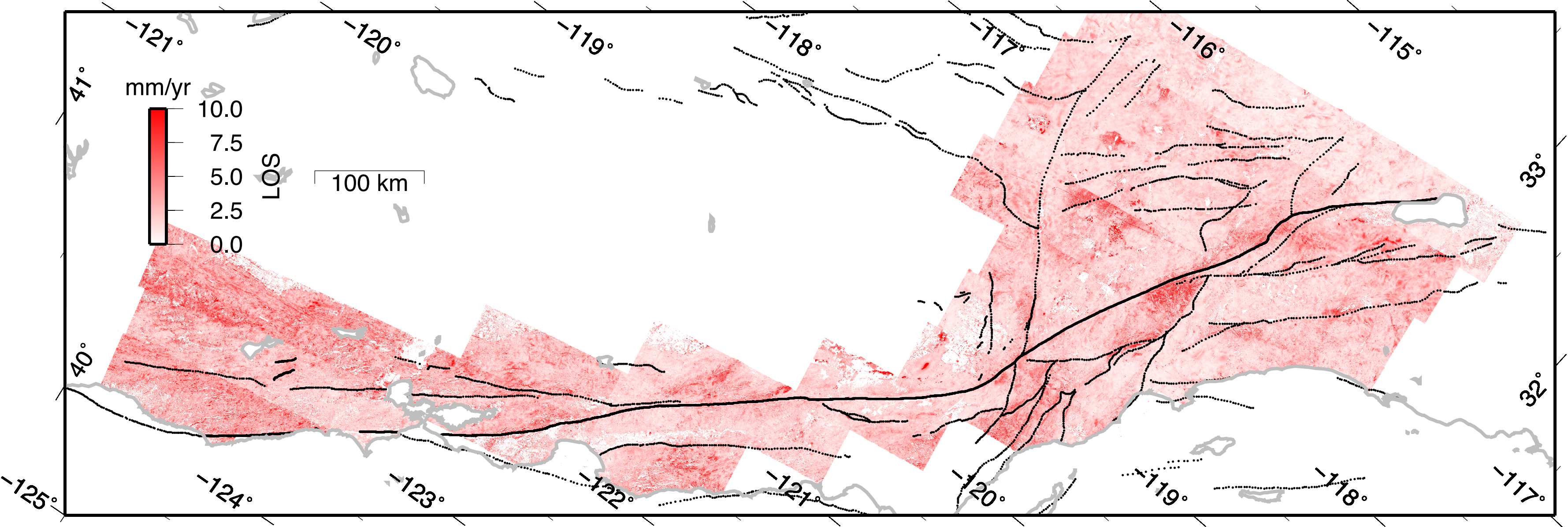
mm/yr
10.0
7.5
5.0
2.5
0.0
LOS
100 km
−121°
−120°
−119°
−118°
−117°
−116°
−115°
41°
40°
33°
32°
−125°
−124°
−123°
−122°
−121°
−120°
−119°
−118°
−117°

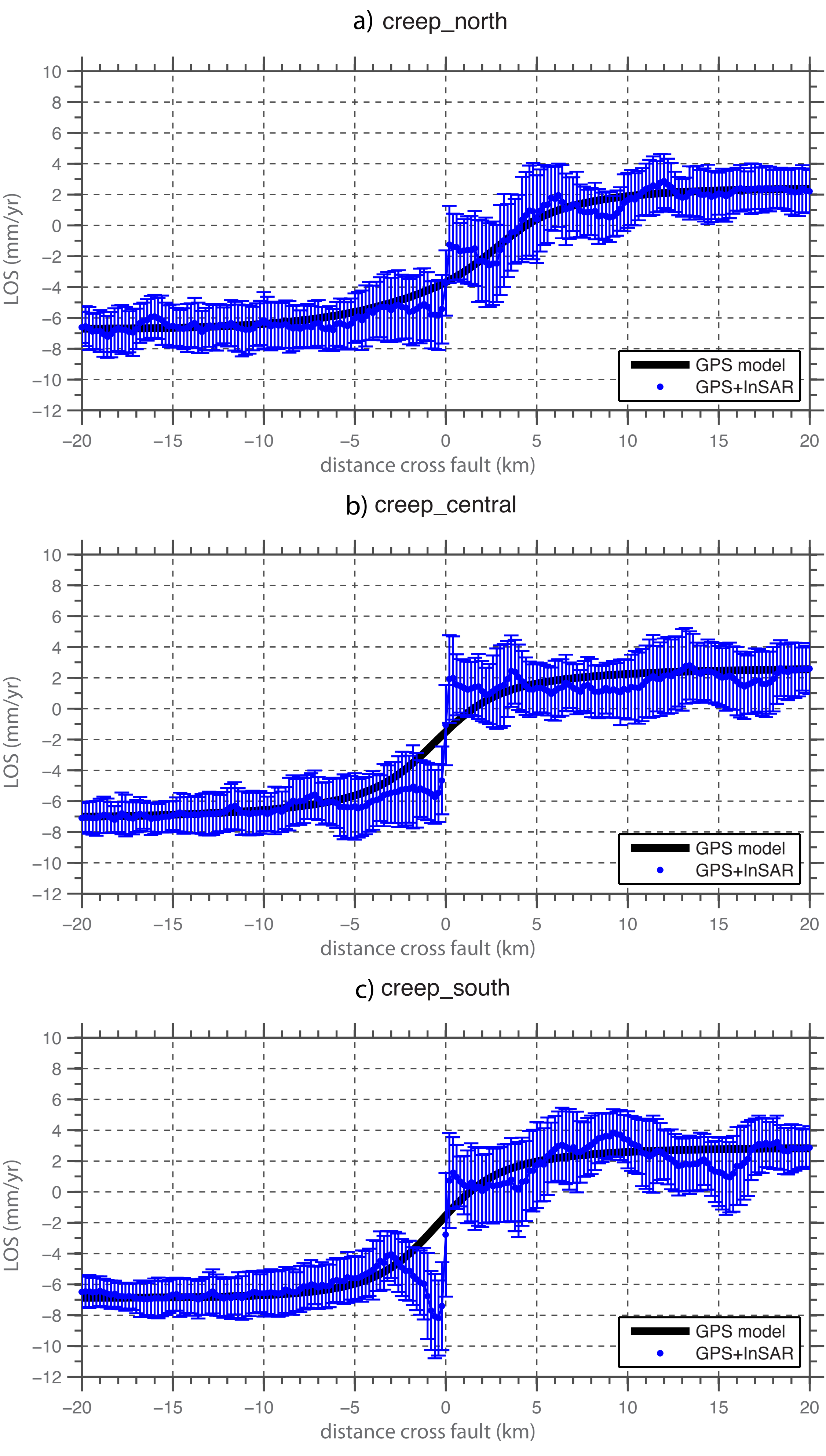
a) creep_north
b) creep_central
c) creep_south
LOS (mm/yr)
distance cross fault (km)
GPS model
GPS+InSAR
10
8
6
4
2
0
−2
−4
−6
−8
−10
−12
−20
−15
−10
−5
0
5
10
15
20

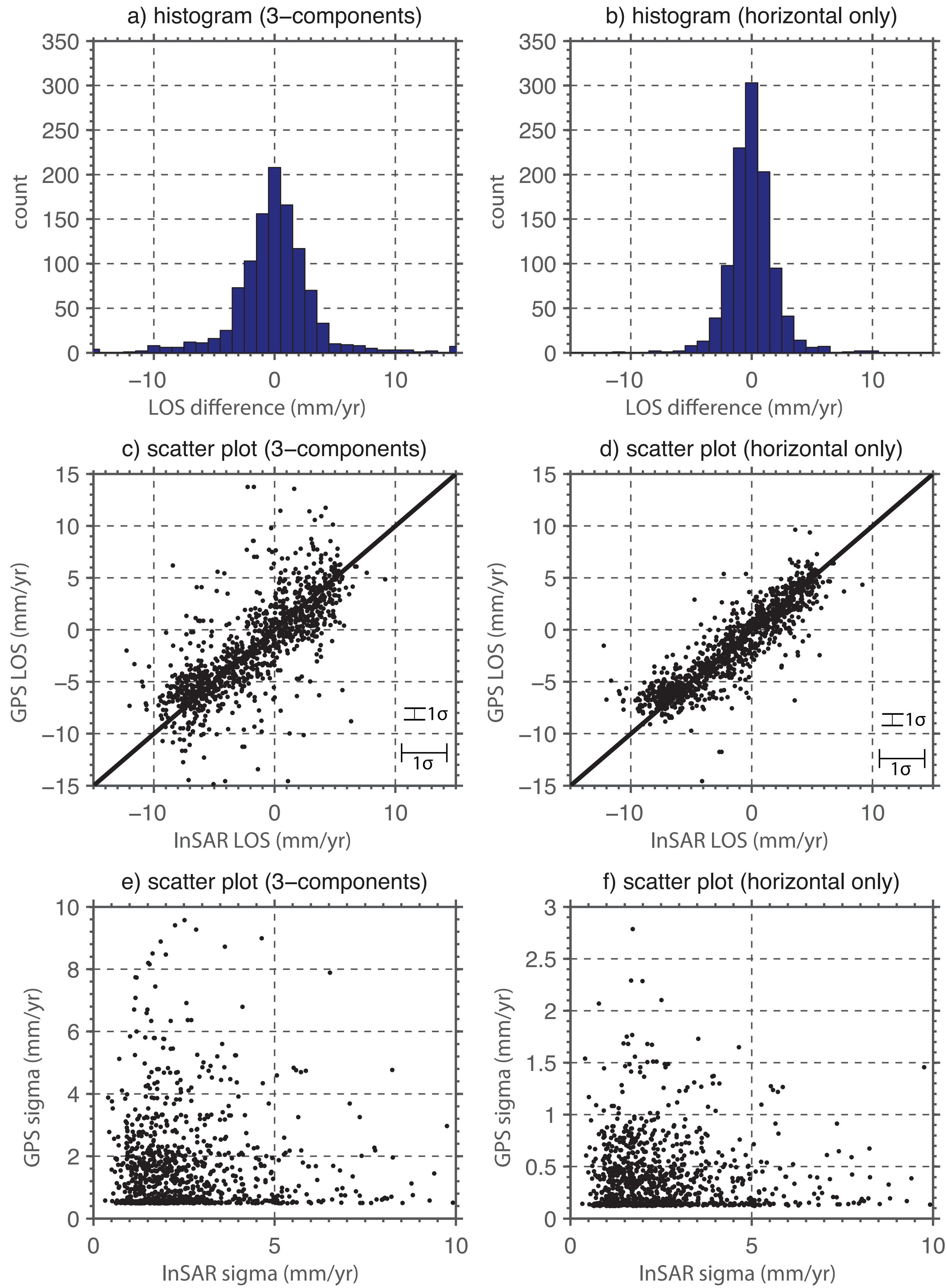

a) histogram (3−components)
b) histogram (horizontal only)
count
LOS difference (mm/yr)
c) scatter plot (3−components)
d) scatter plot (horizontal only)
GPS LOS (mm/yr)
InSAR LOS (mm/yr)
1σ
e) scatter plot (3−components)
f) scatter plot (horizontal only)
GPS sigma (mm/yr)
InSAR sigma (mm/yr)

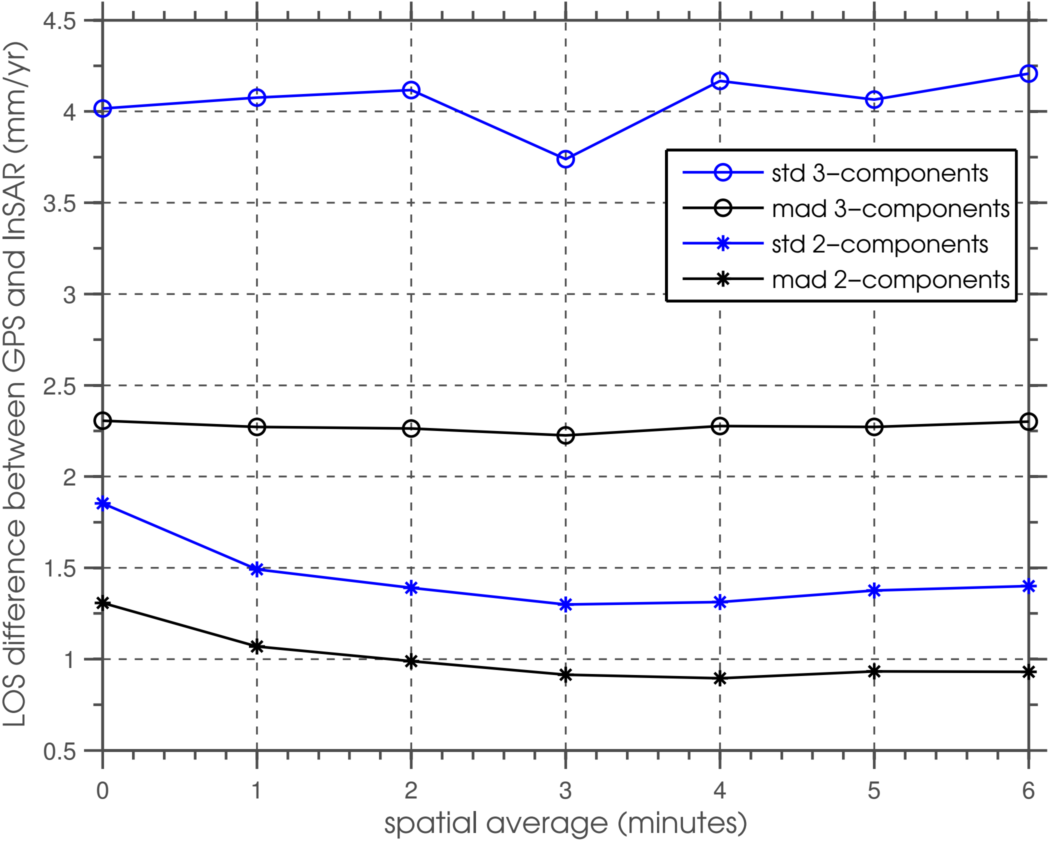

LOS difference between GPS and InSAR (mm/yr)
4.5
4
3.5
3
2.5
2
1.5
1
0.5
0
1
2
3
4
5
6
spatial average (minutes)
std 3−components
mad 3−components
std 2−components
mad 2−components

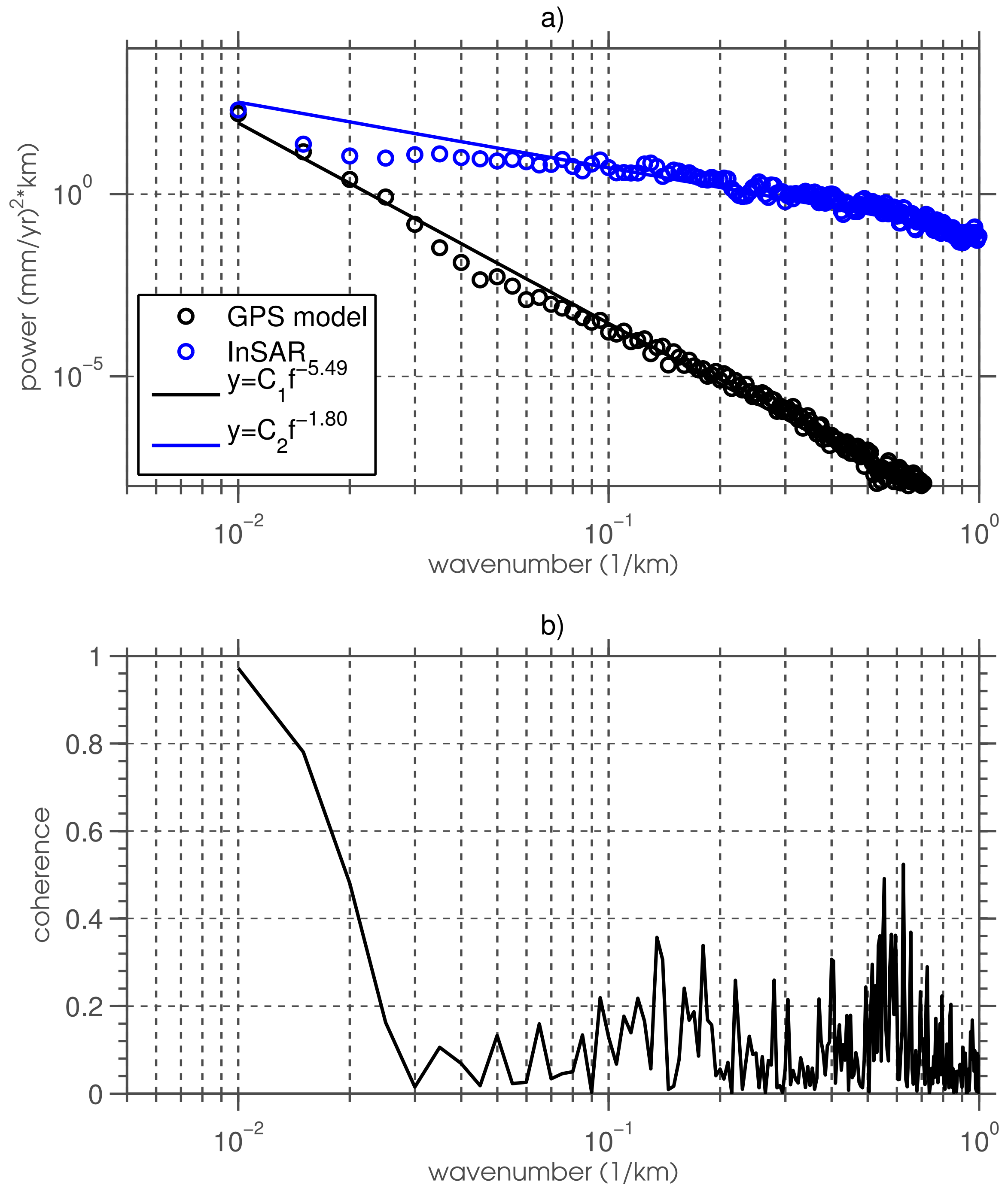

a)
power (mm/yr)^2*km)
10^0
10^−5
10^−2
10^−1
10^0
wavenumber (1/km)
GPS model
InSAR
y=C_1f^−5.49
y=C_2f^−1.80
b)
coherence
1
0.8
0.6
0.4
0.2
0
10^−2
10^−1
10^0
wavenumber (1/km)

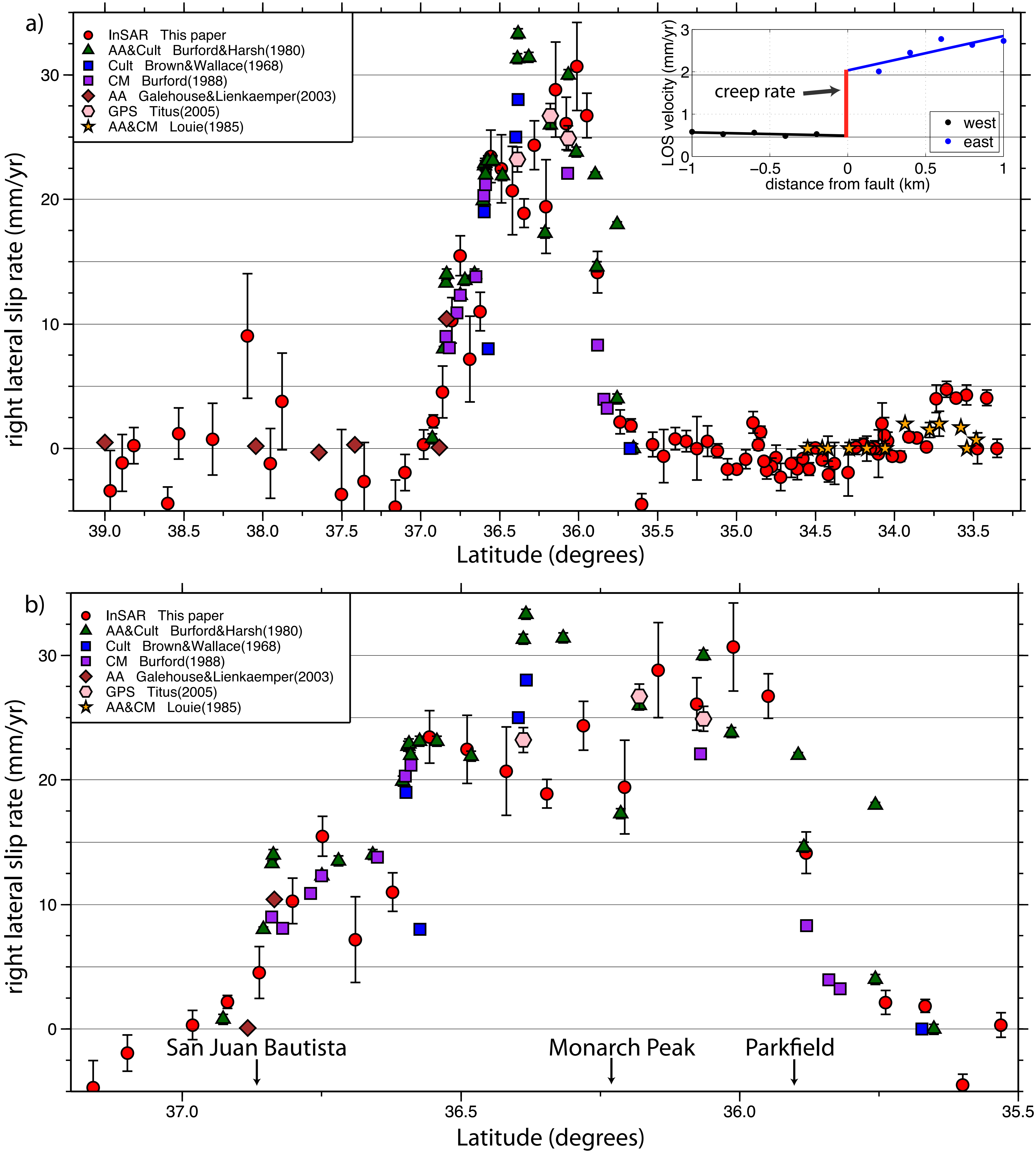
a)
InSAR This paper
AA&Cult Burford&Harsh(1980)
Cult Brown&Wallace(1968)
CM Burford(1988)
AA Galehouse&Lienkaemper(2003)
GPS Titus(2005)
AA&CM Louie(1985)
creep rate
LOS velocity (mm/yr)
distance from fault (km)
west
east
right lateral slip rate (mm/yr)
Latitude (degrees)
b)
InSAR This paper
AA&Cult Burford&Harsh(1980)
Cult Brown&Wallace(1968)
CM Burford(1988)
AA Galehouse&Lienkaemper(2003)
GPS Titus(2005)
AA&CM Louie(1985)
San Juan Bautista
Monarch Peak
Parkfield
right lateral slip rate (mm/yr)
Latitude (degrees)

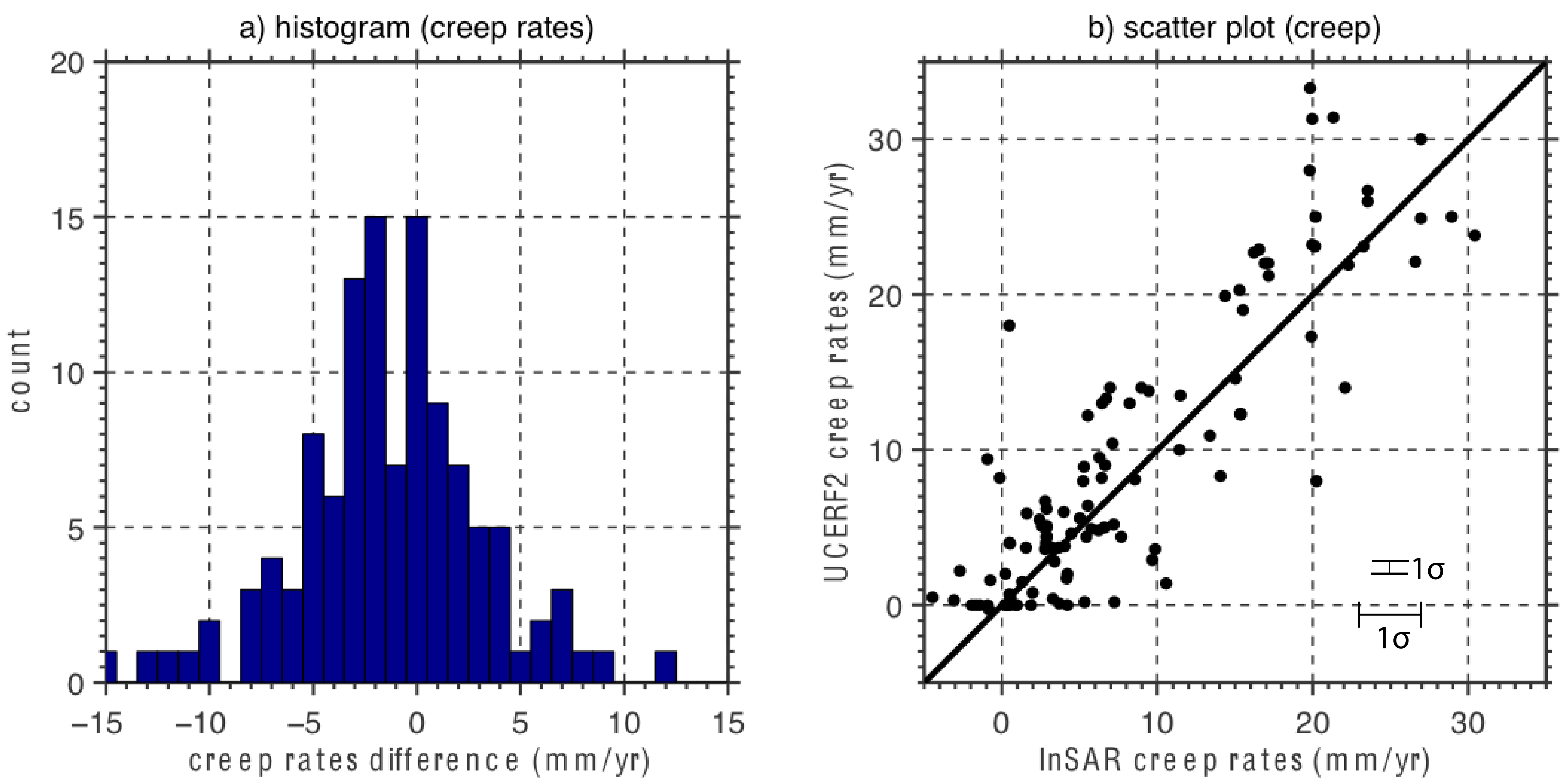
a) histogram (creep rates)
count
creep rates difference (mm/yr)
b) scatter plot (creep)
UCERF2 creep rates (mm/yr)
InSAR creep rates (mm/yr)
1σ
1σ

Painted Canyon GPS survey